Geophysical Journal International

Geophys. J. Int. (2014) **196,** 1544–1563
Advance Access publication 2013 December 30

doi: 10.1093/gji/ggt356

Self-induced seismicity due to fluid circulation along faults

Hideo Aochi,[1] Blanche Poisson,[1,†] Renaud Toussaint,[2,3] Xavier Rachez[4] and Jean Schmittbuhl[2]

[1]*Risks and Prevention Division, BRGM, 3 avenue Claude Guillemin, BP*36009*, Orléans Cedex 2, France. E-mail: h.aochi@brgm.fr*
[2]*Institut de Physique du Globe de Strasbourg, CNRS UMR*7516*, University of Strasbourg, 5 Rue René Descartes, F-*67084 *Strasbourg Cedex, France*
[3]*Center for Advanced Study at the Norwegian Academy of Science and Letters, Drammensveien* 78*,* 0271 *Oslo, Norway*
[4]*Geothermal Department, BRGM, 3 avenue Claude Guillemin, BP*36009*, Orléans Cedex 2, France*

Accepted 2013 September 3. Received 2013 September 2; in original form 2013 April 8

SUMMARY

In this paper, we develop a system of equations describing fluid migration, fault rheology, fault thickness evolution and shear rupture during a seismic cycle, triggered either by tectonic loading or by fluid injection. Assuming that the phenomena predominantly take place on a single fault described as a finite permeable zone of variable width, we are able to project the equations within the volumetric fault core onto the 2-D fault interface. From the basis of this 'fault lubrication approximation', we simulate the evolution of seismicity when fluid is injected at one point along the fault to model-induced seismicity during an injection test in a borehole that intercepts the fault. We perform several parametric studies to understand the basic behaviour of the system. Fluid transmissivity and fault rheology are key elements. The simulated seismicity generally tends to rapidly evolve after triggering, independently of the injection history and end when the stationary path of fluid flow is established at the outer boundary of the model. This self-induced seismicity takes place in the case where shear rupturing on a planar fault becomes dominant over the fluid migration process. On the contrary, if healing processes take place, so that the fluid mass is trapped along the fault, rupturing occurs continuously during the injection period. Seismicity and fluid migration are strongly influenced by the injection rate and the heterogeneity.

Key words: Permeability and porosity; Fracture and flow; Fault zone rheology; Earthquake dynamics; Rheology and friction of fault zones.

1 INTRODUCTION

Some seismicity is believed to be driven by fluid circulation, because high-pressure fluid in the fault zone can reduce frictional strength. In principal, the following two categories can be identified. The first of these is naturally occurring induced seismicity, including volcanic seismicity, some aftershocks of large earthquakes or seismicity in subduction contexts where large quantities of fluid can be expected to be present. In such examples, although the existence of the fluid can be imaged from seismic tomography, it is very difficult to quantify fluid migration and the resultant seismicity. The second category is identified as anthropogenically induced seismicity, forced by industrial or other forms of man-made injection or extraction of fluid, such as the extraction of natural gas, CO_2 storage and the development of deep geothermal systems.

Many cases of naturally occurring induced seismicity have been reported over recent decades. One notable example was the Matsushiro earthquake swarm that lasted 2 yr starting in 1965 and featured more than 60 000 felt earthquakes, the largest of which had a magnitude of 5.4. Although various models based on dilatancy and magma intrusion had been proposed, the events can more probably be ascribed to a massive migration of fluids, including outflow to the ground (e.g. Ohtake 1976; Matsu'ura & Karakama 2005; Cappa *et al.* 2009). Some seismic activities triggered in the wake of large earthquakes suggest the important role of fluids, as demonstrated as far away as 1250 km from the epicentral zone in the wake of the 1992 Landers, California, earthquake (Hill *et al.* 1993). Such triggered earthquake swarms have been observed for other earthquakes too, such as the Yalova cluster that ensued after the 1999 Izmit earthquake (Karabulut *et al.* 2011) or regional seismicity following the 1997–1998 Umbria-Marche, Italy, sequence (Lombardi *et al.* 2010). Earthquake migrations have also been observed as a result of the release of CO_2-rich water (Miller *et al.* 2004). Some crustal earthquakes may have been triggered due to high pore pressure, as inferred for the 2009 L'Aquila, Italy, earthquake (Terakawa *et al.* 2010). Furthermore, the importance of the existence of fluids has been emphasized for plate boundaries, in particular, for

†Deceased 2011 December 8.

subduction associated with microseismicity or aseismic slip. Obara (2002) reported that the discovered deep, non-volcanic tremors along the subducting Philippine Sea Plate may be related to the fluid generated by dehydration processes from the slab. In many cases, the existence of fluid is inferred from seismic tomography as an anomaly of V_p/V_s, the ratio of *P*- and *S*-wave velocities (O'Connell & Budiansky 1974; Thurber *et al*. 1997 and others). Seismicity clusters attributed to fluid migration have also been observed in stable tectonic contexts, such as Remiremont, France (Audin *et al.* 2002).

On the other hand, it is recognized that seismicity can be induced directly in conjunction with fluid injection (Shapiro *et al*. 1999; Shapiro & Dinske 2009), in particular, in deep geothermal projects (Person 1981; Cornet & Jianmin 1995; Calò *et al*. 2011) or CO_2 injection projects (Cappa & Rutqvist 2011a, 2012; Mazzoldi *et al.* 2012; Zoback & Gorelick 2012). The stimulation phases of the deep geothermal projects, in particular, require seismogenic reactivation of pre-existing fractures or microfracturing to allow fluid circulation in the targeted reservoir. Assessing this type of seismicity is, therefore, becoming an important issue. For example, at Soultz-sous-Forêts (Alsace, France), an Enhanced Geothermal System (EGS) has been monitored since an initial borehole drilled to a depth of 2000 m in 1987 (Beauce *et al*. 1991; Kappeimeyer *et al*. 1991; Fabriol *et al*. 1994; Evans *et al*. 2005; Neuville *et al.* 2009; Gentier *et al*. 2011a,b; Evans *et al.* 2012). Subsequently, deeper wells were drilled to depths of about 5000 m, and several stimulations were conducted at regular intervals after 2000 (Dorbath *et al*. 2009). An injection experiment typically lasts a few days (about 100–250 hr), with a maximum injected fluid volume speed of 50 L s^{-1} and wellhead pressure of 17 MPa. The total volume of injected fluid amounts to about 20 000–30 000 m^3. More than 100 000 seismic events were detected in the course of the three stimulation experiments, with rates up to 8000 events per day (Baisch *et al*. 2010). Typically, the seismicity is localized as a cloud surrounding the injection point, which spatially expands with time (Shapiro *et al*. 1999). Sometimes a quiet zone appears around the injection point once it has been sufficiently stimulated, while the fluid and seismicity migrate outside. This is known as the Kaiser (1950) effect. Although the seismicity briefly expands in a complex 3-D medium, the relocated earthquake locations seem to align along a few planes, construed to be pre-existing faults at the site (Dorbath *et al.* 2009; Baisch *et al*. 2010).

Naturally triggered or anthropogenically induced seismicity models have been developed by various researchers in seismology, rock mechanics and other areas of specialization. For injection experiments, volumetric models (sometimes containing networks of linear or plane fractures) have been considered (Bruel 2002, 2007; Gentier *et al*. 2011a,b). However, if the seismicity occurs predominantly along some pre-existing fault(s), a linear fault (in 2-D) or a plane fault (in 3-D) are often studied (e.g. Blanpied *et al.* 1992; Segall & Rice 1995; Baisch *et al*. 2010; Cappa & Rutquist 2011b, 2012). Fault rheology is a key element allowing fluid transport. Early models of fluid-driven seismicity triggering simply considered the pressure balance in broken portions to be instantaneous, corresponding to an assumption of very high porosity in these sections (Miller *et al.* 1996). Since natural materials mostly give rise to low Reynolds numbers, due to their low porosity, more precise models incorporate a finite viscosity and pore-fluid transport through permeable parts (governed by Darcy's law, e.g. Walder & Nur 1984). When finite compressibility of the fluid plays a role, it is reported that this leads to associated pore pressure diffusion (Shapiro *et al*. 1999; Goren *et al*. 2010, 2011). This compressibility is shown to be involved in most systems of shear faults, and must be taken into account to understand the evolution of pore pressure around the fault (Goren *et al*. 2010).

Experimentally, fracturing and finger propagation during fluid injection in analogue faults have been observed at the laboratory scale, in transparent impermeable cells filled with granular materials comparable to fault gouge (Johnsen *et al*. 2006, 2008a; Cheng *et al.* 2008; Huang *et al.* 2012a,b). Similar pattern formations were observed after injection of a slightly compressible and viscous fluid (oil), and of a compressible and slightly viscous substance (air) (Johnsen *et al*. 2008b)—as was the case for the formation of decompaction fronts in such systems (Vinningland *et al.* 2012). The fracturing and fingering triggered by fluid injection was shown experimentally to be accompanied by microseismicity (Schelstraete 2009).

To address this type of fluid-driven fracturing, modelling the momentum exchange between the flowing fluid and the elastic solid is essential. When the two are considered as distinct, continuous bodies, mixture theories have been developed that are widely used to model wet landslides (Iverson 1997). In the context of high fluid flow in highly deformable solids, similar momentum exchanges have been considered between the fluid and discrete element models (Flekkøy *et al.* 2002; Johnsen *et al.* 2006). These models have been shown to closely reproduce experimental results, for the deformation of both granular materials saturated with compressible fluids (Vinningland *et al.* 2007a,b, 2010) and incompressible ones (Niebling *et al.* 2010a,b, 2012a,b). In this study, we will explicitly take into account the momentum exchange (drag) between the fluid and the deformable solid, considering the finite compressibility and the viscosity of the fluid. An important difference, enabling us to address large systems, is that the solid will be treated here as a continuum with a fault gouge rheology.

In this study, we build a conceptual simulation model to take into account elastic and plastic porosity changes (e.g. Segall & Rice 1995) and fault width evolution (e.g. Yamashita 1999), assuming that the fluid flow and seismicity expand predominantly along a fault plane in a 3-D medium. In particular, we address the issue of how induced seismicity, once initiated on a fault, can be brought under control. As we aim to model microseismicity, we treat the coseismic rupture process as simply as possible by solving the static equilibrium equations of the elastic medium. In this respect, the approach for the pore pressure and solid stress computations is similar to models developed for fluid injection by Rozhko (2010). Thus, we are not introducing any coseismic thermal effects (Andrews 2002), which are often discussed for 'large' natural earthquakes with large fault slip. The lubrication effect due to pressurized fluid during unstable stages of the dynamics can also be taken into account dynamically (Rice 2006; Segall & Rice 2006; Brantut *et al.* 2011), coupling the fluid dynamics with a discrete elements model to represent the solid (Goren *et al.* 2011; Ghani *et al.* 2013).

2 THE MODEL

2.1 Conceptual model of a fault zone

The geological structure and mechanical properties of the earthquake faults have been studied by field observations and drillings for certain active faults (e.g. Chester *et al.* 1993; Caine *et al.* 1996; Lockner *et al.* 2009). The fault core consists of: a rupture trace, surrounded by fault gouge, a damage zone and the surrounding host rock (Fig. 1). The hydraulic properties also vary from the fault centre (core) to the host rock.

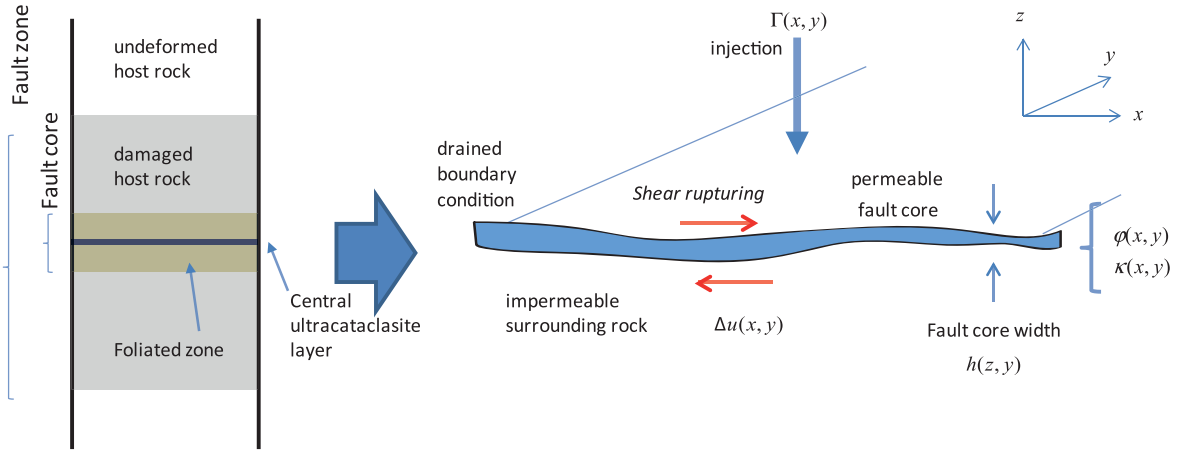

Figure 1. Conceptual illustration of fault internal structure (after Chester *et al.* 1993) and our model allowing fluid circulation and induced seismicity predominantly along a pre-existing 2-D fault plane with a fault core of width $h(x, y)$. The fault core is surrounded by impermeable rock. Fault slip is given by $\Delta u(x, y)$ directed along the x-axis, so that the shear stress $\tau(x, y)$ of interest is a xz-component. The pore pressure in the fault core $P(x, y)$ can evolve due to the injection $\Gamma(x, y)$, as a function of the variable fault constitutive parameters of porosity $\phi(x, y)$ and permeability $\kappa(x, y)$.

In this study, we will not be considering the poroelastic or the granular nature of the fault core and damage zone. Let us assume that fluid is only allowed within the permeable fault core (e.g. Segall & Rice 1995; Rice 2006). We also assume a variable finite width h of the fault core (Yamashita 1999), as shown in Fig. 1. We take the fault core thickness into account when dealing with fluid behaviour, but we consider this thickness to be small enough compared to the fault length for us to be able to calculate the elastic response of the medium due to shear rupture. We then consider that the fluid only circulates in the fault core and that the pore pressure reduces the effective normal stress applied on the fault (as observed at the scale of the fault thickness for impermeable lateral walls, see Goren *et al.* 2011, among others). Shear rupture is assumed to be described by the Coulomb criterion (e.g. Terzaghi 1943). The rupture may change the state of the poroelasticity (e.g. porosity, permeability and fault width) of the fault core, but we assume that fluid flow and poroelastic response occur at very different timescales and can accordingly be solved sequentially (see numerical algorithm of Fig. 2).

The system of the governing equations for fluid migration in any porous medium is commonly based on two equations: first, the linear Darcy's law if the Reynolds number is sufficiently low (e.g. Chapman 1981):

$$\vec{q} = -\rho \frac{\kappa}{\eta} \nabla P, \tag{1}$$

which indicates that fluid mass flux $\vec{q}$ [kg s^{-1} m^{-2}] is proportional to the gradient of fluid pressure with fluid density ρ, fluid viscosity η and permeability κ; and, secondly, the continuity of fluid mass:

$$\nabla \cdot \vec{q} + \frac{\partial (\rho\phi)}{\partial t} = \rho \dot{\Gamma}, \tag{2}$$

where ϕ is porosity and $\dot{\Gamma}$ is the fluid source (volumetric injection rate).

One of the rheological models most frequently called upon is taken from Walder & Nur (1984) and Segall & Rice (1995), who write the change in porosity as the sum of elastic and plastic components:

$$\frac{\mathrm{d}\phi}{\mathrm{d}t} = \dot{\phi}_{\mathrm{elastic}} + \dot{\phi}_{\mathrm{plastic}} = \frac{\partial \phi_{\mathrm{elastic}}}{\partial P} \frac{\partial P}{\partial t} + \dot{\phi}_{\mathrm{plastic}} = \phi \beta_\phi \dot{P} + \dot{\phi}_{\mathrm{plastic}}, \tag{3}$$

where β_ϕ is the elastic pore compressibility defined by $\beta_\phi = (1/\phi)(\partial\phi/\partial P)$. Strictly speaking, the quantityβ_ϕ should represent the reversible poroelastic characteristic of the medium in the case where $\partial\phi_{\mathrm{plastic}}/\partial P = 0$. Combining the above equations, we obtain:

$$\dot{P}(x, y, z) = \frac{1}{\phi(\beta_f + \beta_\phi)} \left[\nabla \left(\frac{\kappa}{\eta} \nabla P \right) - \dot{\phi}_{\mathrm{plastic}} + \dot{\Gamma} \right], \tag{4}$$

corresponding to eq. (12) in Segall & Rice (1995), eq. (1a) in Wong *et al.* (1997), eq. (1) in Miller & Nur (2000) and eq. (7) in Goren *et al.* (2010).

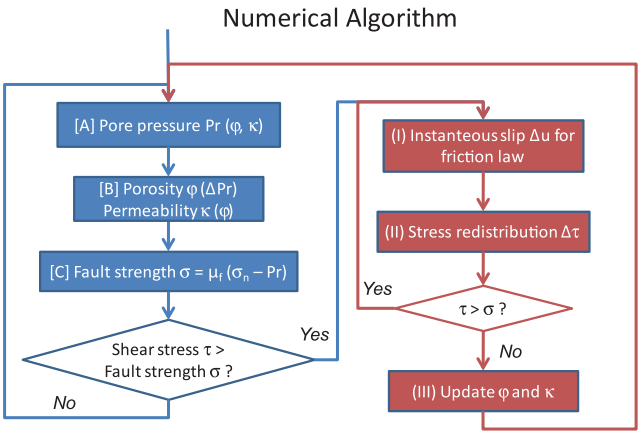

Figure 2. Numerical algorithm used in this study. In the left-hand side, the loop is concerned about the fluid circulation. Once the rupture criterion is reached (left bottom), the rupture process is solved at the right-hand side. Every time, fault property (porosity and permeability) may evolve.

2.2 Fault zone boundary condition and governing equation

In this study, we consider that the permeability κ varies along the (x,y)-fault plane as shown in Fig. 1. We then integrate eq. (4) over the fault-perpendicular direction (z) for the fault zone as demonstrated in Yamashita (1999). We assume that the fluid does not flow across

the interface between the fault core zone and the surrounding, low-permeability rock, at $z = h_+$ and h_-, and that inside the fault core zone, the variables are uniform in the z-direction, as variation along this direction is considered to be smaller than in the (x, y) directions:

$$\int_{h-}^{h+} (\nabla \vec{q} + \dot{m})\, \mathrm{d}z = \int_{h-}^{h+} \rho \dot{\Gamma}(x, y, z)\, \mathrm{d}z, \tag{5}$$

which leads to:

$$h\left(\frac{\partial q_x}{\partial x} + \frac{\partial q_y}{\partial y}\right) + [q_z]_{h-}^{h+} + h\dot{m} = \rho h \dot{\Gamma}, \tag{6}$$

where the fault core width is expressed by $h = (h_+) - (h_-)$. Note that, all the variables are hereafter averaged within the fault core and are functions of (x, y) only. There is no perpendicular flux across the fault boundary due to the impermeability of the surrounding medium, but it is related to the change of the boundary position itself, as follows:

$$q_z = \rho\phi \frac{\mathrm{d}h}{\mathrm{d}t}. \tag{7}$$

We then obtain:

$$h\left(\frac{\partial q_x}{\partial x} + \frac{\partial q_y}{\partial y}\right) + \rho\phi \frac{\mathrm{d}h}{\mathrm{d}t} + h\frac{\mathrm{d}}{\mathrm{d}t}(\rho\phi) = \rho h \dot{\Gamma}. \tag{8}$$

The product of the permeability κ and fault width h is called 'transmissivity', which is often used to describe the horizontal water flow in aquifers (e.g. Zimmerman & Bodvarsson 1996; Zimmerman & Main 2004). However, for our application, the shear rupturing may greatly change the characteristics of the fault zone in terms of the porosity of the fault core and the fault zone width. If either of these two parameters is unchanged during the process, we could adopt the transmissivity as a model parameter. Now the equation is reduced to a 2-D problem (i.e. lubrication approximation). We can, therefore, similarly write, according to eq. (4):

$$\dot{P}(x, y) = \frac{1}{\phi(\beta_f + \beta_\phi)}\left[\nabla\left(\frac{\kappa}{\eta}\nabla P\right) - \phi\frac{\dot{h}}{h} - \dot{\phi}_{\text{plastic}} + \dot{\Gamma}\right]. \tag{9}$$

This relation is to be compared with eq. (4) with an additional term including h.

The mass of the medium should be conserved regardless of the change in porosity:

$$\frac{\mathrm{d}}{\mathrm{d}t}\left((1-\phi)\rho_\phi h\right) = 0, \tag{10}$$

where ρ_ϕ is the density of medium and then, again using $\beta_\phi = (1/\phi)(\partial\phi/\partial P)$, we obtain the evolution for h:

$$\dot{h} = h\left(\frac{\dot{\phi}}{1-\phi} - \beta_\phi \dot{P}\right). \tag{11}$$

Compared to the equation in Yamashita (1999), our boundary condition is defined differently so that the conservation of mass is taken into account. Yamashita (1999) treated the fault core width as an independent variable but in our formulation it depends on the other variables, porosity and pressure.

2.3 Rupture process and stress redistribution

As previously stated, the rupture process is governed by a Coulomb law. An increase in pore pressure plays a role in reducing the fault strength. The fault strength τ_f is expressed as:

$$\tau_f = \mu_s \sigma_n^{\text{eff}} = \mu_s(\sigma_n - P), \tag{12}$$

where μ_s is the static frictional coefficient and σ_n^{eff} is termed effective normal stress, or Terzaghi's normal stress (Terzaghi 1943). The fact that this effective stress controls shear rupture via a Coulomb law was experimentally established in triaxial laboratory tests, for example, by Nur & Byerlee (1971). The rupture does not begin if the applied shear stress is lower than the strength. During the rupture, the fault strength reduces gradually with on-going slip (Δu) after a characteristic distance (so-called 'slip-weakening distance' and usually called D_c) to the residual stress (dynamic friction) level (Ida 1972; Palmer & Rice 1973; Ide & Takeo 1997; Ohnaka 2003; many others). This weakening process is often written as a simple equation, such as:

$$\tau(\Delta u) = \tau_d + (\tau_f - \tau_d)\left(1 - \frac{\Delta u}{D_c}\right) H\left(1 - \frac{\Delta u}{D_c}\right), \tag{13}$$

where $H(x)$ is the Heaviside function: $H(x \geq 0) = 1$, otherwise 0. The residual strength (dynamic stress) τ_d is given through a dynamic friction coefficient μ_d ($\mu_d < \mu_s$):

$$\tau_d = \mu_d \sigma_n^{\text{eff}} = \mu_d(\sigma_n - P). \tag{14}$$

The strength drop during an event is accordingly:

$$\Delta\tau = \tau_f - \tau_d = (\mu_s - \mu_d)(\sigma_n - P), \tag{15}$$

if the effective stress does not change during this event. Comparing the fault-weakening process during an earthquake, the healing process is not well known. Usually, it is considered that the fault heals over time and shear strength is progressively recovered (Dieterich 1972). However, the simplest, often-used approximations, which are also the most extreme, are immediate healing or no healing.

Eq. (13) describes the relation between the on-going slip and strength evolution on the fault. Slip generated on a fault element causes stress increases in the surrounding, so-called 'stress redistribution'. For simplicity, the stress redistribution is calculated as a static dislocation problem in an infinite, homogeneous 3-D elastic medium, a common procedure in seismology. We regard the shear rupturing as occurring in a very narrow trace within the fault zone. The static response function (Green's function) can be obtained analytically from the equilibrium equation of elasticity. The discretization on square subfaults is summarized in Appendix A according to Tada *et al.* (2000). Tada *et al.* (2000) integrated the elastodynamic equations by parts (renormalization process) so as to avoid the strong singularity when estimating stress values along the fault. This stress redistribution may let the other fault elements rupture subsequently. We iterate the process one element by another at a time until all the elements are found to be stable (the imposed stress including the initial one and the perturbation coming from the others is lower than the strength at that time). At last, we can evaluate the seismic moment of one event through the traditional definition used in seismology (e.g. Kanamori & Anderson 1975):

$$M_0 = \mu \sum_i \Delta u_i \Delta s^2, \tag{16}$$

where Δu_i is the instantaneous fault slip at this time step for ruptured fault element i, and Δs^2 is the element's surface. One can follow the overall fault evolution with the cumulative fault slip over time.

2.4 Fault porosity and permeability

The link between porosity and permeability plays a crucial role. The permeability value depends strongly on the material and fracture network. Previously, Gentier *et al.* (2011a,b), for example, found

κ of an order of 10^{-10} m^2 for a fracture network of the Soultz-sous-Forêt EGS site. Such a large effective permeability indicates that the network is relatively well developed due to fractures and pre-existing fault networks. In laboratory experiments on porous materials, permeability is often about 10^{-18} to 10^{-12} m^2 (strongly dependent on the grain size distribution; e.g. Kozeny 1927; Carman 1937; Løvoll *et al.* 2004; Johnsen *et al.* 2006; Mavko *et al.* 2009), and thus the fault in the field must be highly fractured. However, the microscopic rheology that links local porosity and permeability is quite complex, involving plastic deformation processes that are difficult to describe (e.g. Bernabé *et al.* 2003). The relations between porosity and permeability are often power laws (e.g. Brace 1977; Wong *et al.* 1997), while they may change drastically from one state to another due to the rupturing process (Miller & Nur 2000). The permeability and the porosity describing the fault state may change according to the fluid migration as well as shear rupturing (Fig. 2). This is a key point of the discussion in this study.

3 PARAMETER STUDIES

3.1 Model setting and model parameters

In order to understand the behaviour of our model, this section presents a parametric study. The model parameters we employ are summarized in Table 1. We set an injection rate ($\dot{\Gamma}$) of 31.5 [l s^{-1}] during the first 24 hr, for a fault plane consisting of 100 × 100 elements (3000 m × 3000 m). Such an injection rate is quite common for EGSs during the stimulation phases (Evans *et al.* 2012). The injection point, where the injection rate is $\dot{\Gamma}$, is at the fault's centre (everywhere else, the injection rate is nil). The element size is taken to be 30 m, which limits the minimum size of possible earthquake in the simulation scheme. One may question the resolution given by these parameters; this is discussed in Appendix B. The slip-weakening distance D_c is taken as small enough so that this quantity is practically negligible for the used element size (see also in Appendix B). At the model boundaries of the given fault plane, we assume drained conditions.

3.2 Finiteness of fault core width

We first study some simple situations to understand the role of certain parameters. Let us assume that the permeability is uniform and unchanging, regardless of the fault behaviour and fluid migration (Table 2). In eq. (3), we permit the elastic change of porosity ($\dot{\phi}_{\rm elastic}$), but assume no plastic change ($\dot{\phi}_{\rm plastic} = 0$). The fault width is allowed to vary following eq. (11). We test three different initial fault widths of $h_0 = h|_{t=0}$ =1, 3 and 5 m as the models H1, H3 and H5 shown in Fig. 3. We should bear in mind that the fault width h behaves as a scale factor with respect to the permeability κ. In this configuration, fluid behaviour is not linked with fault shear rupture (see also a snapshot at time t = 80 000 s). First, based on the assumed injection, pore pressure continues to increase at the fault's centre. Then it decreases to zero after the end of the injection according to the diffusion term of eq. (9) and a drained condition at the model boundaries. From a physical point of view, pore pressure cannot be allowed to increase above a certain level. The upper limit, therefore, is set at 40 MPa in these simulations in order to guarantee that the effective stress remains positive. Physically, this represents a hydraulic fracture mechanism, where the confining walls of the fault fracture at this value limit the pressure at this saturation level. Numerically, when P exceeds the upper limit, we impose $\dot{P} = 0$. Consequently, the system absorbs the fluid mass change by increasing the fault width h. This type of feedback should operate automatically in real cases. In model H1 (h_0 = 1 m) in Fig. 3(a), the pore pressure immediately rises to the imposed upper value (i.e. when we do not apply this upper limit, the pore pressure exceeds the confining pressure). A significant increase in fault width (of about 10 per cent) and porosity (300 per cent, also imposed as an upper limit) are necessary to absorb the injected fluid mass, while those changes are negligible for the other two cases.

Seismicity is triggered by an increase in pore pressure; that is, the peak shear stress required for rupture decreases versus the injection in model H3 (h_0 = 3 m) in Fig. 3(b). But soon the shear stress increase comes to play a role in subsequent rupturing. In the shown example, the main swarm of seismicity ends with the largest event of $M_{\rm w} \sim 4.3$ (ruptured dimension is 7.7 km^2, or 8558 elements). After the largest event, moderate seismicity continues and then decays slowly. The final event occurs half an hour after the injection has stopped in the case of h_0 = 3 m. Several earthquakes have a magnitude of $M_{\rm w} \sim 1.4$, corresponding to the imposed minimum possible dimension of the potentially ruptured fault segment in the model, set to Δs = 30 m.

When the fault width is large enough (model H5: h_0 = 5 m in Fig. 3c), we observe that the fluid circulates rapidly without any

Table 2. Three fault parameters in the first examples.

Parameter	Initial value	Evolution allowed
Fault width h	1, 3 or 5 m	Variable
Permeability κ	10^{-13} m^2	Invariable, constant
Porosity ϕ	0.05	Variable only by elastic change

Table 1. Model parameters.

Parameter	Quantity
Element size Δs	30 m
Time step Δt	1 s
Fluid viscosity η	2×10^{-4} Pa.s
Fluid density ρ	1×10^3 kg m^{-3}
Fluid compressibility $\beta_{f\varphi}$	5×10^{-10} Pa^{-1}
Elastic medium compressibility β_φ	5×10^{-11} Pa^{-1}
Injection rate Γ	31.5 [l s^{-1}] during the first 24 hr
Rigidity of elastic medium μ	30 GPa
Normal stress (confining pressure) $\sigma_{\rm n}$	100 MPa
Background pore pressure	30 MPa
Static friction coefficient $\mu_{\rm f}$, $\mu_{\rm f}'$	0.65 (for the first rupture), 0.6 (for the rest)
Dynamic friction coefficient $\mu_{\rm d}$	0.55
Critical slip displacement D_c	<0.001 cm

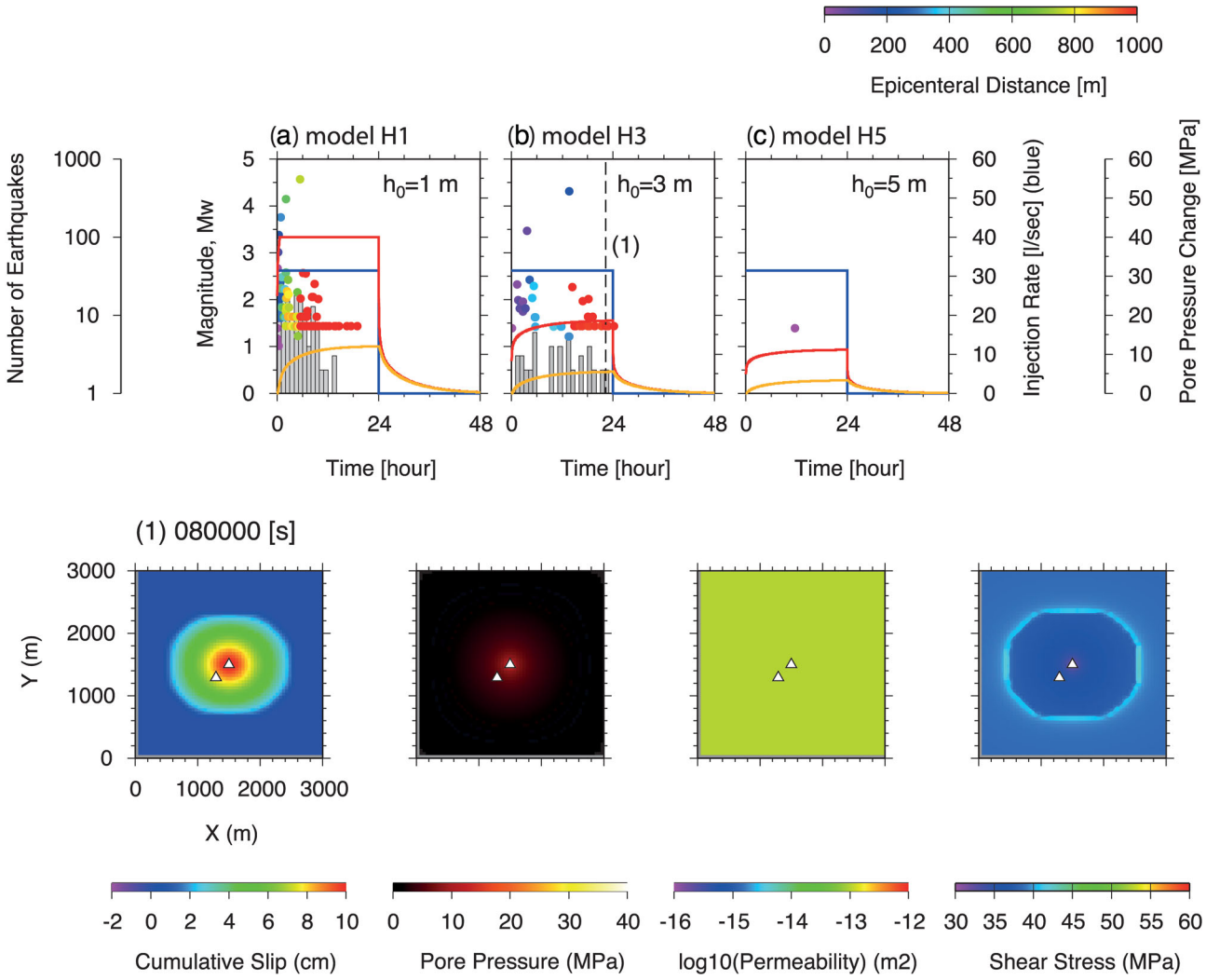

Figure 3. Simulated seismicity versus time in the case of invariable permeability ($\kappa = 10^{-13}$ m^2) for different initial fault widths (h_0) of 1, 3 and 5 m, in (a) model H1, (b) model H3 and (c) model H5, respectively. The seismicity is plotted by dots, coloured to reflect the epicentral distance from the injection point, and the number of earthquakes per hour is also shown in the form of histograms. The injection rate is indicated by blue lines. The pore pressure, represented by red and orange curves, corresponds to two different spots, the injection point (x, y) = (1500 m, 1500 m) and another point (1290 m, 1290 m), respectively; their position is indicated by triangles in a snapshot (cumulative slip, pore pressure, permeability and shear stress) at time $t = 80\,000$ s, indicated by a line (1).

significant pore pressure increase. Thus, significant seismicity is not induced by the fluid injection. Achieving this condition is the objective of industry-related fluid circulation. However, since we are interested in how the seismicity evolves in our formulated system, we adopt the case of $h_0 = 3$ m as our reference for discussing the effects of various parameters and mechanics. We note here for our later discussion that the permeability κ is required to be an order of 10^{-13} m^2 for a fault width of $h = 3$ m for the shear rupturing to occur without increasing the pore pressure by too much (Table 2).

3.3 Permeability evolution

The fault property (porosity and permeability) evolves with time following the rupturing. In eq. (3), the first term originating from the elastic change of the porosity ($\dot{\phi}_{\rm elastic}$) is practically negligible, because it is estimated as of an order of 10^{-4} [s^{-1}] for a porosity of 0.1 and a numerically possible change in pressure ($\dot{P}$) of 10^7 [MPa s^{-1}]. As seen in the later simulations, pressure changes are never so rapid in the considered cases. Therefore, the second term ($\dot{\phi}_{\rm plastic}$) may play a practical role, but the definition of $\dot{\phi}_{\rm plastic}$ still remains quite uncertain. Segall & Rice (1995) introduced a relation that is analogous to the state variable evolution of the rate- and state-dependent friction law. Yamashita (1999) describes the plastic porosity as slip (Δu)-dependent:

$$\phi_{\rm plastic} = \phi_{ss} + \Delta\phi \exp(-\Delta u/u_c), \tag{17}$$

where ϕ_{ss}, $\Delta\phi$ and u_c are constant. Besides, the relation between the permeability and the porosity may be written as (e.g. Brace 1977):

$$\kappa = \kappa_0(\phi/\phi_0)^n, \tag{18}$$

where κ_0, ϕ_0 and n are constant. We tried to use these relations (Appendix C). However, the permeability does not always increase significantly and thus the pore pressure tends to increase easily in eq. (9), namely the insufficient increase in the porosity (the terms $\nabla((\kappa/\eta)\nabla P)$ and $\dot{\phi}_{\rm plastic}$) does not always cancel the injection term ($\dot{\Gamma}$). In other words, alternative evolution of κ is necessary due to the external conditions (rupturing, stress, etc.) rather than the internal relations, such as eqs (17) and (18).

Therefore, we adopt the toggle switch (e.g. Miller & Nur 2000) in which the permeability changes independently from the change in porosity. For simplicity, we introduce two irreversible phases locally according to the state of the fault at each point, that is, intact or already ruptured:

$$\kappa(x,y) = \begin{cases} 10^{-14} m^2 & \text{for } u(x,y) = 0 \\ 10^{-13} m^2 & \text{for } u(x,y) \neq 0 \end{cases}, \tag{19}$$

where u is the cumulative slip ($u = \sum \Delta u$). Thus, the value is initially small everywhere, and once rupture has occurred, permeability increases up to a constant value of 10^{-13} m^2. The value of 10^{-14} m^2 assigned to the material before shear rupture took place might be much smaller as in granular materials; however, the simulation is not influenced, as the given value is quite small so that the fault is practically impermeable at the timescale of our interest. No plastic change in porosity is assumed ($\dot{\phi}_{\text{plastic}} = 0$), as the permeability is no longer related to the porosity. The term $\nabla((\kappa/\eta)\nabla P)$ is dominant in eq. (9). We show the simulation results (hereafter referred as model K2) in Fig. 4. The other parameters are the same as for model H3 in Fig. 3(b). As the pore pressure increases along the boundary of permeability contrast, that is, at the front of the rupture zone,

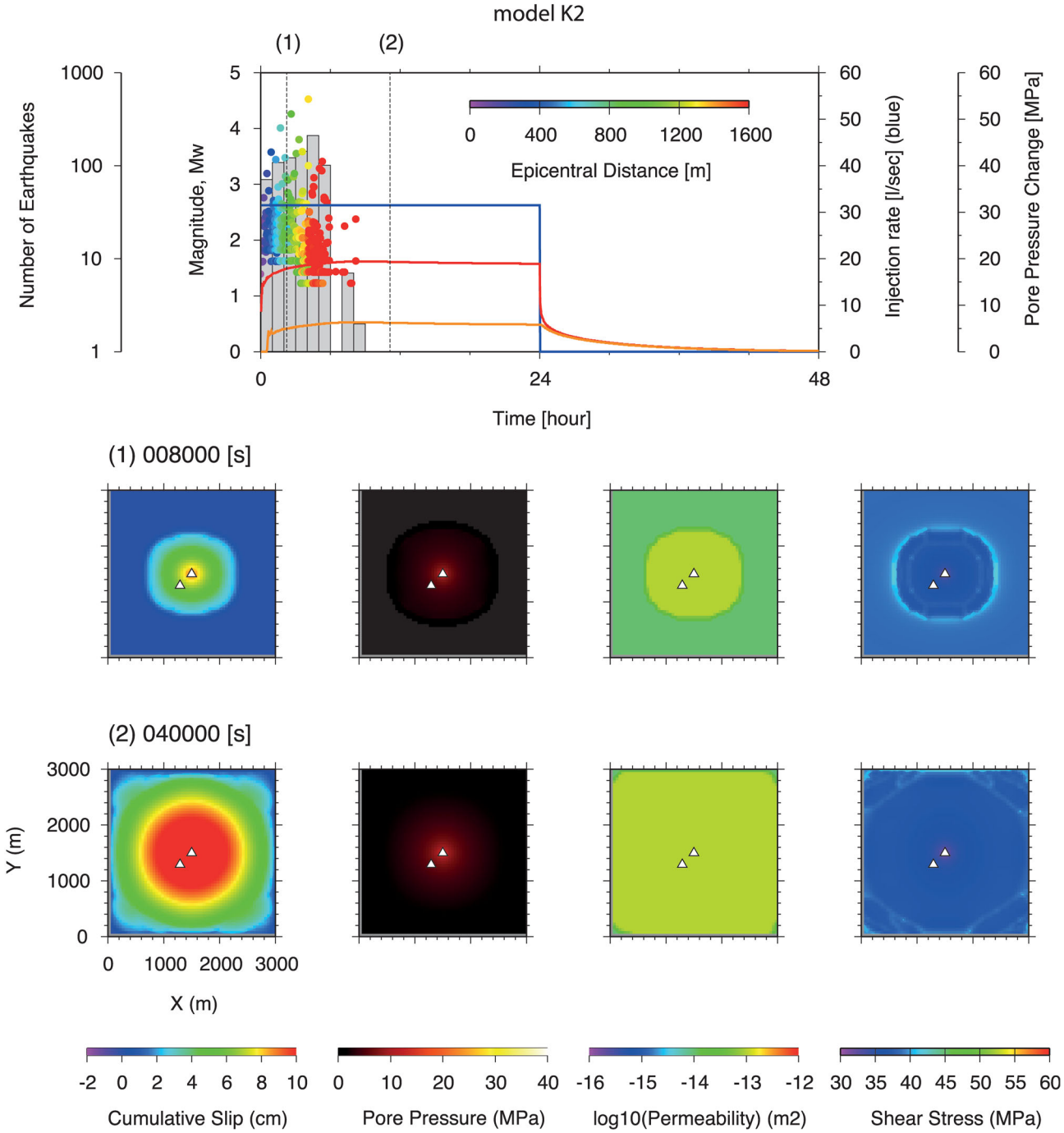

Figure 4. Simulated seismicity with variable permeability. Hereafter, it is referred as model K2. Snapshots are shown at two different times, labelled (1) and (2). See also the caption for Fig. 3.

seismicity migrates away from the injection point. Seismicity is far more pronounced than model H3 in Fig. 3(b): the rupture front advances gradually, step by step. The pore pressure does not increase beyond the rupture front due to the low permeability, so that it is difficult for rupture to occur there, while in the previous case, the pore pressure increases over a wide area. The assumption of such an abrupt change in permeability due to fracturing leads to seismicity being caused by fluid migration as the injection continues.

3.4 Heterogeneity in stress field and fault strength

The origin of the heterogeneity observed in earthquake dynamics (e.g. Kanamori & Stewart 1978; Aki 1979) is a fundamental question in seismology. Schmittbuhl *et al.* (2006) study the stress field of the Nojima Fault before and after the 1995 Kobe, Japan, earthquake and propose that the fluctuations of the stress field along the fault would be dominated by 'quenched' fault properties rather than dynamic stress fluctuations produced during the earthquake. Let us study the effect of heterogeneity in initial shear stress or in fault strength on the produced seismicity. The meaning of heterogeneity differs for the stress field and the fault strength, since the former can be released by a rupture while the latter may remain indefinitely despite repeated ruptures. We first furnish a heterogeneous shear stress, simply assuming a periodic variation according to a single Fourier mode approach as a first step, although the actual stress field could be a superposition of different characteristic lengths of heterogeneity (e.g. Mai & Beroza 2002):

$$\tau_0 = T_0 \times [1 - \delta \cdot f(x, y)], \tag{20}$$

where $f(x, y) = \sin(2\pi x/\lambda_x + \alpha_x)\sin(2\pi y/\lambda_y + \alpha_y)$ is a function of position (x, y), λ_x and λ_y are the given wavelengths in spatial heterogeneity, and α_x and α_y are random numbers. The variable δ indicates the amplitude of the heterogeneity, namely a ratio with respect to the absolute amplitude. In Fig. 5, we show the simulation results for (a) model K2_ST10 with δ of 10 per cent ($\delta = 0.1$) and (b) model K2_ST20 with $\delta = 0.2$, taking $\lambda_x = 300$ m and $\lambda_y = 500$ m, respectively. Introducing the heterogeneity leads to more overpressure locally and yields more earthquakes comparing to model K2 of Fig. 4. The snapshots are also shown for model K2_ST20 with $\delta = 0.2$ (i.e. 20 per cent) at different times (Fig. 5). The expansion of

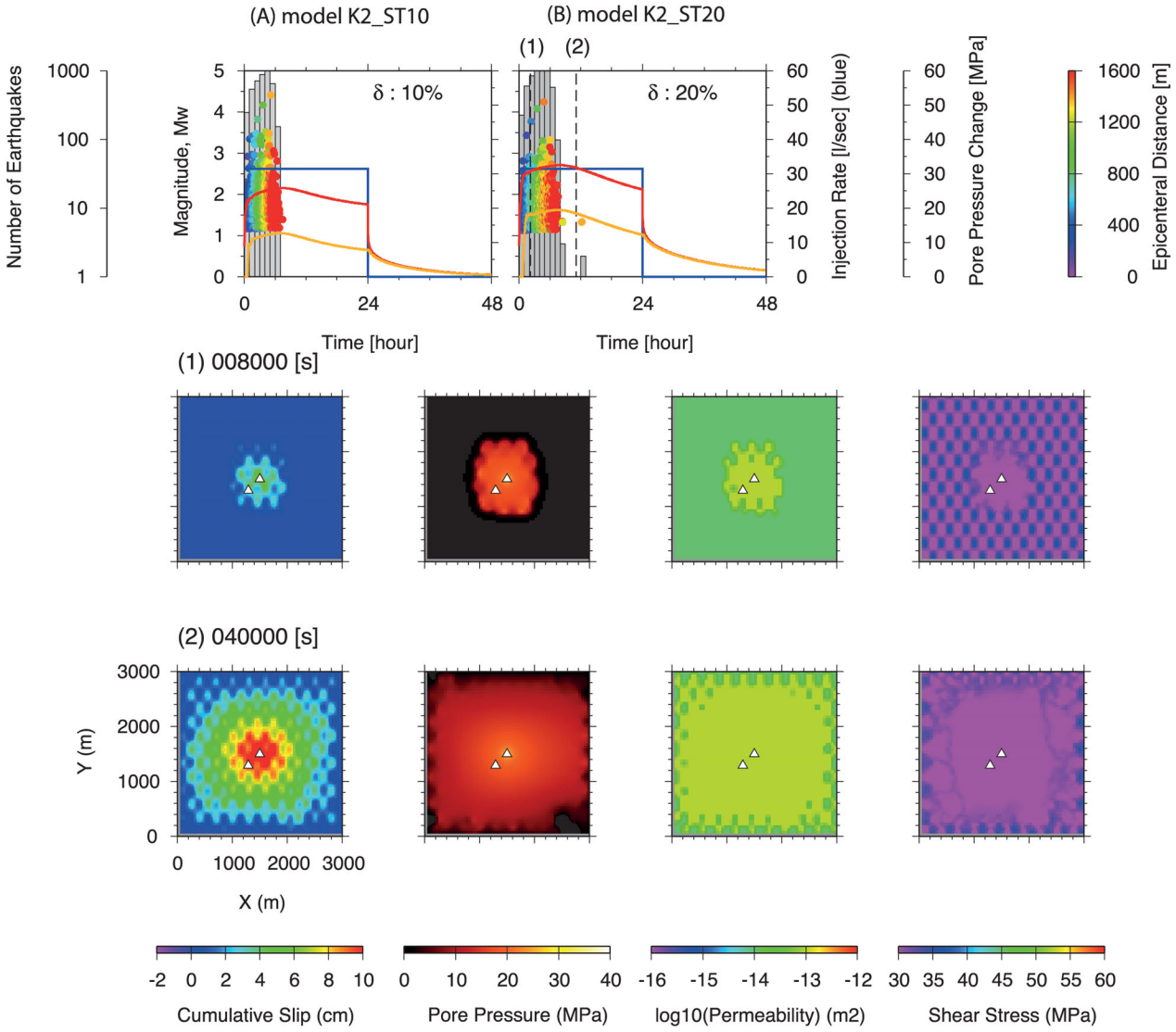

Figure 5. Simulated seismicity for two heterogeneous fields of initial shear stress, (a) model K2_SH10: $\delta = 0.1$ (i.e. 10 per cent) and (b) model K2_SH20: 0.2 (20 per cent). Snapshots are shown at two different times, labelled (1) and (2). See also the caption for Fig. 3.

the ruptured area is heterogeneous and complex in space. In snapshot (1), we note that the area of slip extends slightly further along the y-axis because of the longer wavelength of the heterogeneity. For instance, Perfettini *et al.* (2001) numerically study the correlation of the slip pattern and strength heterogeneity in seismic cycles and find that the slip appearance reflects the background strength heterogeneity. This is also the case in our simulation. When the fault has almost entirely ruptured, the fluid circulation becomes quasi-uniform because of the homogeneous permeability in the ruptured area. At this time, some areas remain unruptured (snapshot at time (2) in Fig. 5).

Similarly, we study the effects of spatial heterogeneity for the other parameters. The fault strength, that is, the static frictional coefficient, is given a variation based on the reference frictional coefficient μ_{s0}:

$$\mu_s(x, y) = \mu_{s0} \times \{1 + \text{ var} \cdot (\mu_{s0} - \mu_d) f(x, y)\}, \tag{21}$$

where the same variation function $f(x, y)$ as in eq. (20) is used. We note that normal stress itself does not change since we are considering a planar fault, but the effective normal stress changes due to the pore pressure change (eq. 12). The dynamic frictional coefficient μ_d is assumed to be uniform everywhere. The relation in eq. (21) represents a continuous change, but we also assume heterogeneity in the discontinuously localized forms:

$$\mu_s(x, y) = \begin{cases} \mu_{s0} \times \{1 + \text{ var} \cdot (\mu_{s0} - \mu_d)\} & \text{if } f(x, y) \geq 0.8 \\ \mu_{s0} & \text{otherwise} \end{cases}. \tag{22}$$

Fault strength after the first rupture is always heterogeneous according to eqs (21) and (22). We show, in Fig. 6, the snapshots for two cases, (a) model K2_TC20 using eq. (21) and (b) model K2_TD20 using eq. (22), with $\delta = 0.5$ (50 per cent), that is, the maximum value of a given μ_s is 0.975. Slightly more earthquakes are observed in model K2_TD20 (b) than model K2_TC20 (a) from the histograms. Behind the rupture front, in model K2_TD20 (b), the heterogeneity remains visible and the overall fault slip is smaller when comparing the two snapshots at $t = 16\,000$ s. From these simulations, we discover that discontinuous localized

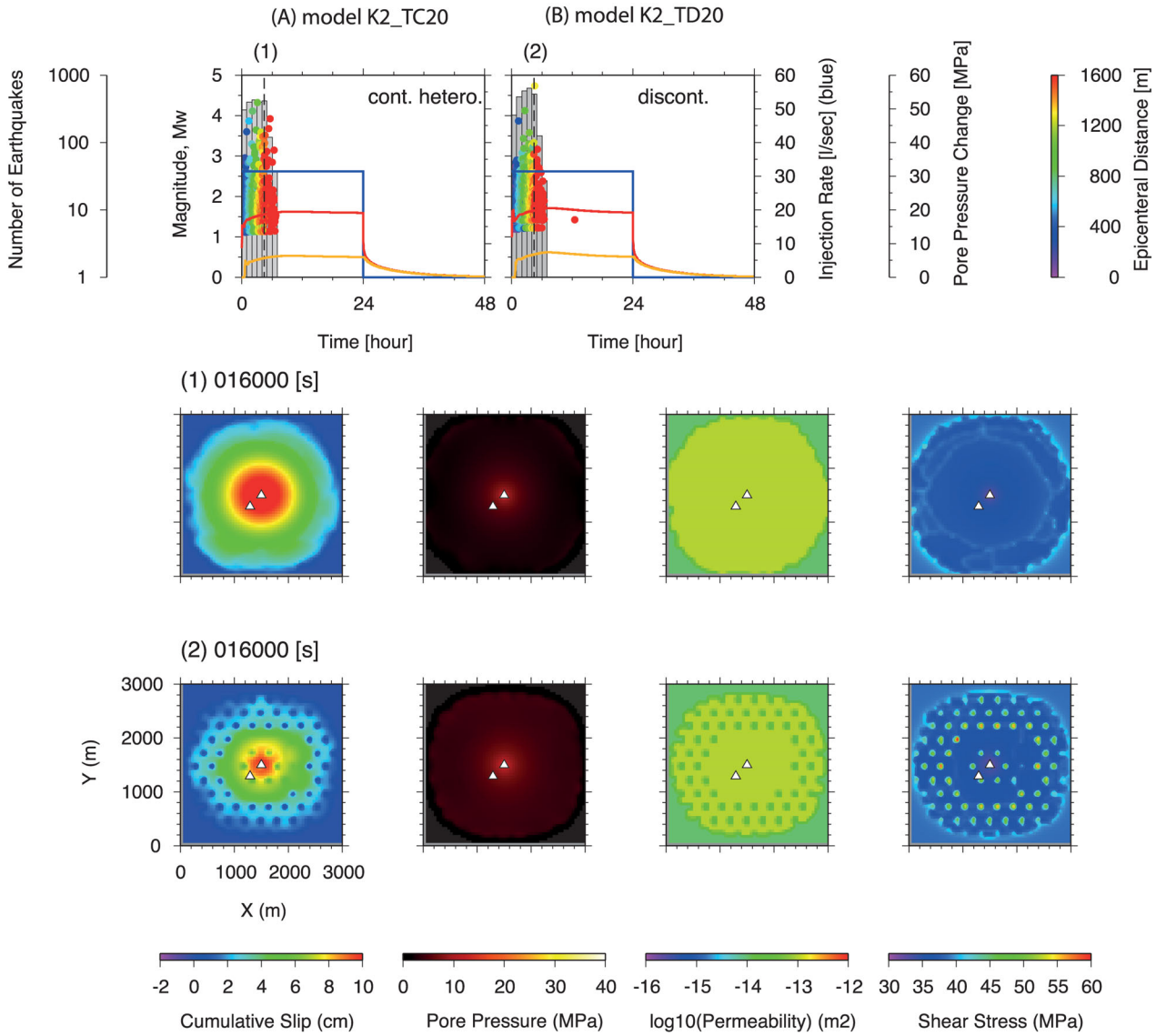

Figure 6. Simulated seismicity for two descriptions of heterogeneous fault strengths, (a) model K2_TC20: spatially continuous, and (b) model K2_TD20: discontinuous cases. Snapshots are shown at two different times labelled (1) and (2). See also the caption for Fig. 3.

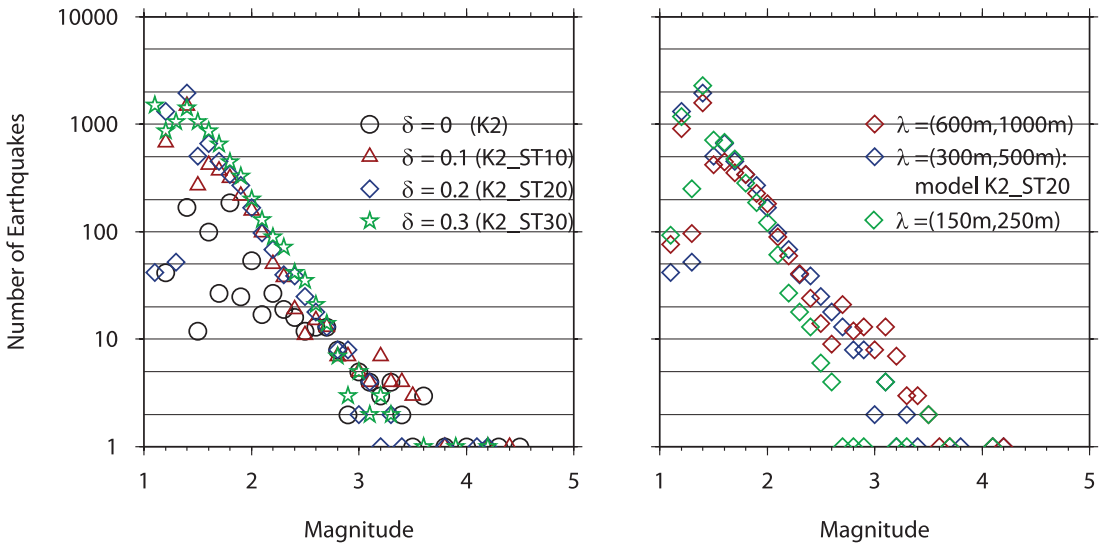

Figure 7. The magnitude–frequency relations for different simulations. The first panel shows four different cases of heterogeneous initial shear stress field, model K2 (Fig. 3), K2_ST10 (Fig. 4a), K2_ST20 (Fig. 4b) and K2_ST30 with $\delta = 0.3$ (30 per cent). The second panel shows the cases of different wavelengths based on K2_ST20.

heterogeneity affects the details of the rupture growth. The rupture front shape becomes very heterogeneous, and heterogeneous slip distribution persists behind the rupture front. As a result, the total slip is reduced.

3.5 The appearance of seismicity

In Fig. 7, we analyse the magnitude–frequency relation from some of the simulated seismicity catalogues. In all cases, we obtain the classic power law relation known as Gutenberg–Richter (Gutenberg & Richter 1954) with a slope of about –1. Large magnitude events have only a single sample for a given magnitude range of 0.1, and they seem to diverge from the power law. However, the ruptured area for large events reaches the model boundary, so this point should be regarded with caution.

In general, the number of earthquakes increases at the same time as larger magnitude earthquakes appear. Pore pressure increases until a large earthquake ($M_w > 4$) occurs, creating a continuous fluid path to the drained model boundary, that is, a breakthrough. Once this happens, the system becomes stable, and the level of seismicity reduces. This silence is somehow an artificial effect, as the size of the maximum event and the ruptured area is limited by the *a priori* model dimension. However, seismic hazard assessment for induced seismicity in geothermal sites is a major concern (e.g. Majer *et al.* 2007; Baisch *et al.* 2009), although phenomena are not completely understandable mechanically (Majer *et al.* 2012).

4 THE POTENTIAL FOR SEISMICITY CONTROL

4.1 The effect of injection and spontaneous seismicity propagation

A challenging question is to find out how the seismicity can be controlled by the injection. We reduced the injection rate by 10 compared with the previous cases and its duration to a few hours instead of one day, expecting to observe an evolution in seismicity (or no seismicity) once injection had ceased.

As shown in Fig. 8, we simulate two cases under the homogeneous condition (a: model K2_I1) similar to model K2 in Fig. 4 and heterogeneous initial shear stress (b: model K2_ST20_I2) like model K2_ST20 with $\delta = 0.2$ (20 per cent) of Fig. 5. The onset of induced

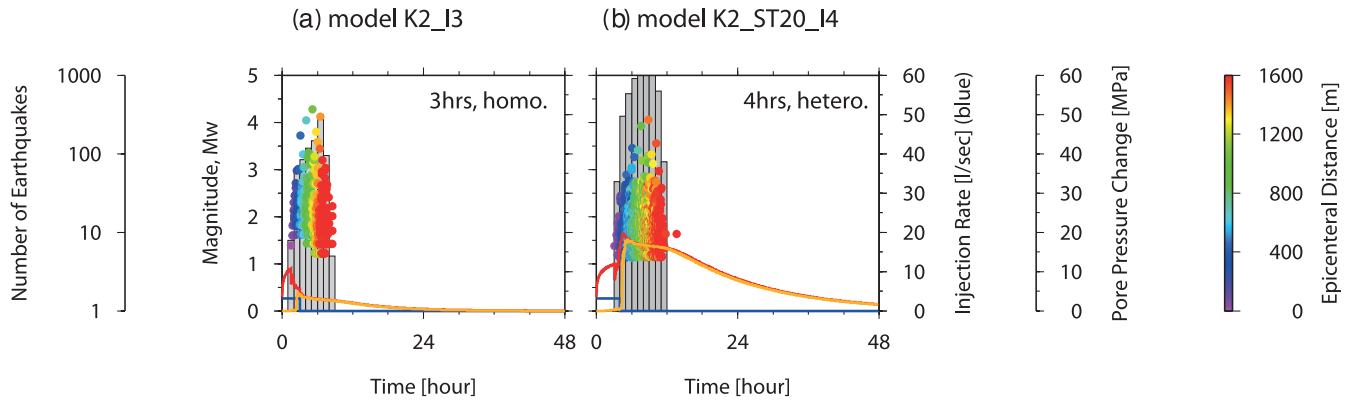

Figure 8. Simulated seismicities for short injection durations. (a) Model K2_I3: 3 hr of injection for the homogeneous condition (the same configuration as model K2 in Fig. 4), and (b) model K2_ST20_I4: 4 hr of injection for heterogeneous condition (*cf.* model K2_ST20 in Fig. 5). The latter case requires a longer injection because the initial shear stress at the injection point happens to be low.

seismicity is delayed simply because it takes much more time for sufficient pore pressure to build up at the injection point, while the duration of seismicity does not change visibly as compared to previous cases. The duration of the injection is 3 and 4 hr, respectively. The difference in injection duration comes simply from the fact that the given heterogeneity (model K2_ST20_I2) needs a greater concentration of pore pressure at the injection point. In both cases, the injection is stopped just after the seismicity began. However, the seismicity continues to propagate and eventually ruptures the entire model fault. We also note that introducing heterogeneity does not affect this rupture expansion, although it does generate much more seismicity and pore pressure remains relatively high. The rupture progress is locally somehow blocked by the heterogeneity but continues on to the end when the fault system is relaxed.

We conclude that it is very difficult to control seismicity through injection under the given conditions. Once induced, the seismicity propagates rather spontaneously, probably because the heterogeneity considered in this study might still be too small in amplitude and too short in its characteristic correlation length of heterogeneity (Perfettini *et al*. 2001). The expansion rate of seismicity is insensitive to differences in injection protocol. The shear rupture spontaneously triggers other ruptures to the surrounding area. In this sense, the seismicity is self-induced once started. The mechanism might be similar to the propagation of solitary dislocation propagation (Schmittbuhl *et al.* 1993), or to Bürgers-like solitons evidenced theoretically for the propagation of overpressure pulses in mud volcanoes (Garcia *et al.* 2000; Revil 2002). The source of this mechanism lies in the non-linear diffusion process for the fluid pressure, arising due to the pressure dependence of the permeability.

4.2 Fault healing and trapped fluid circulation

The real permeability of the fault should be more complex than given by eq. (19). We observe that in all the previous simulations, pore pressure finally drops to zero once injection stops. All the injected fluid flowed out from the model boundary as the fault became sufficiently permeable. In reality, the permeability may decrease over time to disturb the fluid circulation and trap it. Let us, therefore, introduce the temporal evolution (sealing) of permeability relative to fault healing, analogous to Aochi & Matsu'ura (2002):

$$\frac{\mathrm{d}\kappa}{\mathrm{d}t} = -\beta(\kappa(t) - \kappa_\infty), \tag{23}$$

where the parameter $1/\beta$ provides the characteristic time so that the permeability converges to the final value of κ_∞. We do not seek to determine here whether the mechanism of the healing process is mechanical or chemical. For the sake of simplicity, we assume $\kappa_\infty = \kappa(t = 0)$; however, the fault core may take on a new value, different from the initial permeability, because of the development of a microfracture network and the shear rupture. No healing takes place in the limit of $\beta = 0$, and $\beta = 1/(432\,000\ \mathrm{s}) = 1/(5\ \mathrm{d})$ does not produce any visible effect on the simulation. On the other hand, a large β value indicates a rapid healing of the permeability. For example, in the case of $\beta = 1/(60\,\mathrm{s})$, the healing is exceedingly fast, and pore pressure becomes very high at the injection point. In our current system, the fluid circulation is allowed, not during the coseismic event, but after this rupture. However, the permeability becomes low again soon after the rupture. Thus, the fluid circulation is limited. If we allow fluid migration during the event, say $\kappa = \infty$ on the concerned fault segments during rupture (Miller & Nur 2000), it would be possible to introduce an immediate healing process.

In Fig. 9, we show a typical intermediate case of $\beta = 1/(21\,600\ \mathrm{s}) = 1/(6\ \mathrm{hr})$, model K2_B6, under the same conditions as model K2 in Fig. 4. After the first swarm of seismicity terminated by rupture of the entire fault (the first 6 hr), there is a period of quiescence. This quiet period allows time for the fault to heal, specifically because of the decrease in permeability in the fault zone. As a result, the fluid starts to be trapped, and since fluid is continuously injected, seismic activity resumes once again releasing fluid. After the end of the injection, the fluid is not completely drained due to this sealing effect. Thus, the pore pressure remains at a certain finite value. In a natural context, such distinct swarms may not be identified, as the system can be expected to be more complex and heterogeneous than the simplified model (a single, uniform parameter of sealing). The fact that the system transits from a continuous activity to an intermittent one when β increases is the analogue, in induced seismicity, to the transition observed for fault activities under tectonic loading, when the healing process

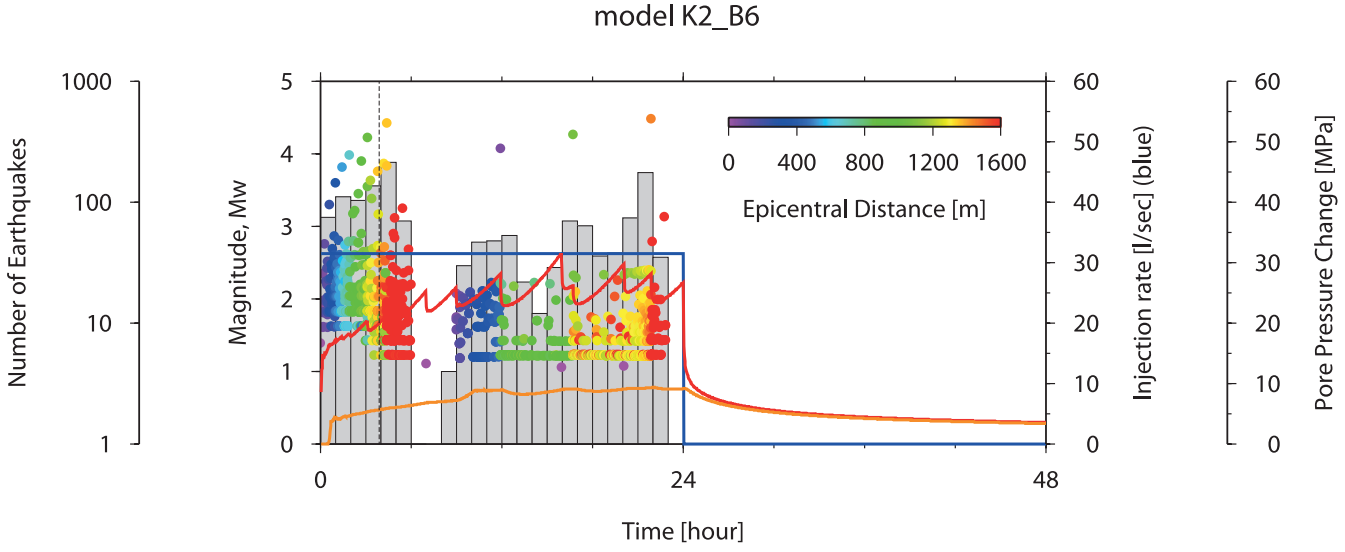

Figure 9. Simulated seismicity for the case of $\beta = 1/(21\,600\ \mathrm{s})$, model K2_B6, for an injection of 24 hr (the same as Fig. 4 except for β).

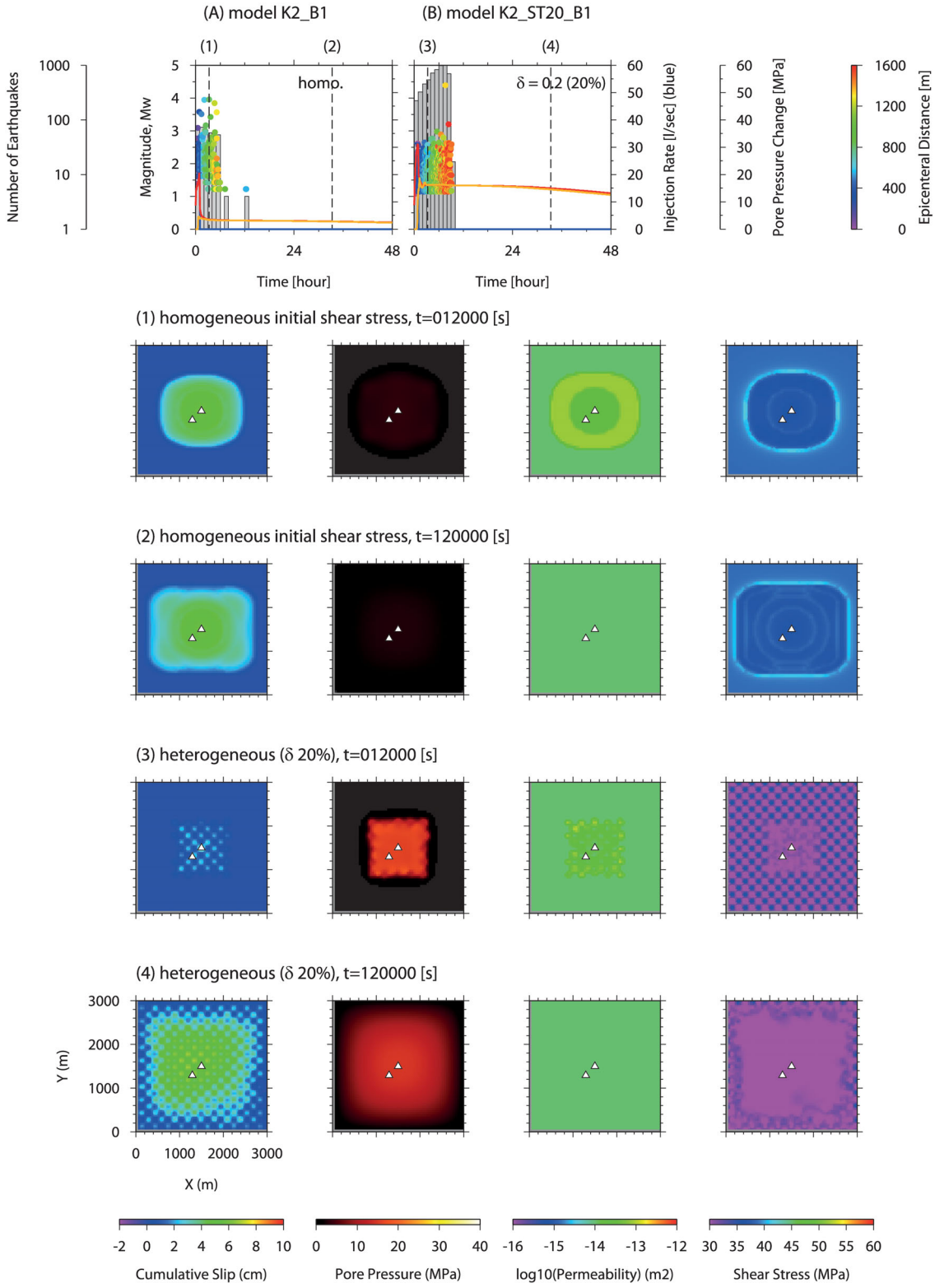

Figure 10. Simulation results for the cases of $\beta = 1/(3600\text{ s})$ for a short injection duration. (a) Model K2_B1: homogeneous, and (b) model K2_SH20_B1: heterogeneous initial shear stresses are given, respectively, letting $\lambda_x = \lambda_y = 300\,\text{m}$. Snapshots are shown for the two different moments for each simulation. In the latter case, the pore pressure is trapped after injection has stopped and the fault is not entirely ruptured.

changes from slow to fast rates—as was observed and explained along the San Andreas Fault (Gratier 2011; Gratier *et al.* 2011).

We now try to emphasize the healing effect on the seismicity and fluid circulation, by reducing the injection time and assuming $\beta = 1/(3600\text{ s}) = 1/(1\text{ hr})$. We test homogeneous and heterogeneous initial shear stress ($\delta = 0.2$) with wavelengths of $\lambda_x = \lambda_y = 300\,\text{m}$, respectively (a: model K2_B1, and b: model K2_SH20_B1 in Fig. 10). This version of the model reproduces the seismicity without

fracturing the whole model fault and the trapped fluid effect without breakthrough. The pore pressure after the end of injection decreases not to zero but to a finite value. Unlike the previous simulations, we also find that heterogeneity plays an important role. In model K2_B1 in Fig. 10(a), homogeneous initial shear stress (the same as for model K2 in Fig. 4 except for β), seismicity gradually but rapidly ceases after the end of the injection (1 hr). In model K2_SH20_B1 (Fig. 10b) employing heterogeneous initial shear stress, it takes a much longer time for the seismicity to subside. The seismicity rate (number per hour) significantly increases after the end of the injection, and we observe an earthquake of magnitude 4.39 triggered close to the model boundary. This significant perturbation can be due to the particular distribution of heterogeneity. However, the seismicity ceases after approximately 9 hr and fluid is ultimately trapped on the healed fault with a relatively high pore pressure.

4.3 Fault interaction

One of the major hypotheses in this study is that the rupture process is restricted to a single-fault plane. In this case, the stress redistribution is carried out strictly following the equations in Appendix A, bringing stress disturbance at any distance. However, as previously treated in Baisch *et al.* (2010), let us assume that the stress disturbance only affects the neighbouring elements, namely $G_{(i-l)(j-m)} = 0$ for $|i - l| > 1$ or $|j - m| > 1$ in eq. (A2). This extreme condition may correspond to a segmentation of the fault off the major plane.

We show an example of seismicity evolution according to the given injection rate (model SB in Fig. 11). This time, rupture is significantly influenced by the injection process despite the fact that the ruptures grows quickly independently of the injection rate. In order to demonstrate how the seismicity is sensitive to the injection protocol, we assume a synthetic injection protocol varying during 2.5 d. We also introduce a relation for the permeability evolution such that it increases by 50 per cent with every rupture until the upper limit. The seismicity increases during the course of the injection and reducing the injection rate decreases the seismicity. When the injection rate increases once again the seismicity starts to evolve. The seismicity continues during the whole duration of the injection and after its end.

The effect of stress redistribution is important in governing the induced seismicity. The structure of natural fault systems can be more complex rather than a single-fault plane. It is worth pointing out that stress redistribution on a single planar fault tends to accelerate the rupture growth rapidly, namely 'self-induced' seismicity, independent of the injection protocol.

5 DISCUSSION

A simple spring-block model does not take into account the elastic response at distance, but only distributes the stress over neighbouring elements, so that the initially imposed heterogeneity also generates a strong heterogeneity in stress and fault slip (e.g. Bak & Tang 1989). On the other hand, elastic systems that have remote responses (e.g. Rice 1993) behave in such a way as to homogenize both stress and slip. The friction law assumed in this study does not consider any evolution process during a single coseismic event; that is, it lacks a length scale, such as characteristic slip distance. Thus, inherently, our discrete system might display spatiotemporal complexity, but globally over a large spatial scale and a long timescale, the simulation finishes when the fault has completely ruptured and/or a stationary injection flow is established from the injection point to the outer boundary of the model. All the simulations display spatial migration, with many events statistically reproducing the scheme of the Gutenberg–Richter magnitude–frequency relation. Once seismicity is induced, we see that it is difficult to control because the shear rupture process becomes dominant. This self-induced behaviour is different from any model simulated by a spring-block model of interaction with the immediate neighbourhood (Baisch *et al.* 2010).

We summarize the spatiotemporal evolution of the seismicity simulated in this study (Fig. 12). The seismicity, once induced by the injection, clearly propagates rather spontaneously, independently of the injected fluid in our simulations. Seismicity migration is often represented in the form:

$$r = \sqrt{4\pi Dt}, \tag{24}$$

where r is the distance of the seismicity front from the injection point, t is the time since the injection onset and D is hydraulic diffusivity (e.g. Shapiro & Dinske 2009). Shapiro & Dinke (2009) also report that there are some local clouds presenting a very rapid

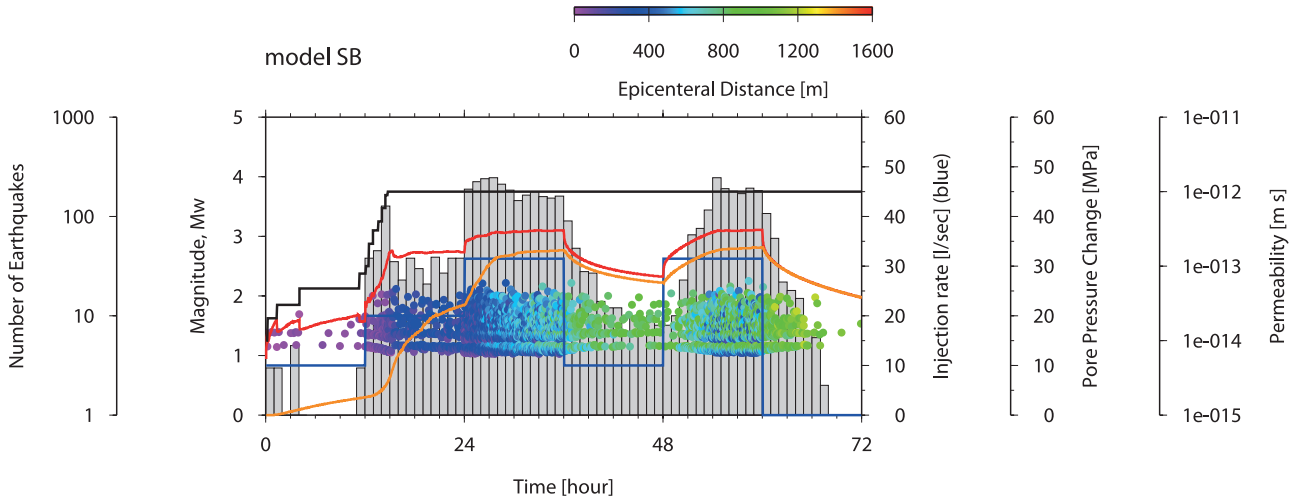

Figure 11. Evolution of seismicity according to varied injection rate with time (model SB). The stress redistribution affects only the adjacent elements and the permeability changes evolutionally every event.

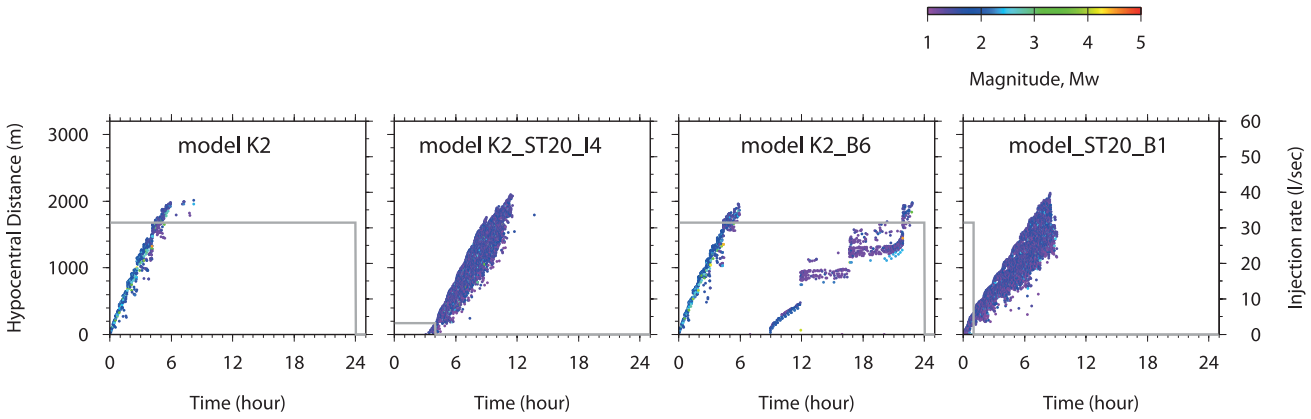

Figure 12. Evolution of seismicity for the four cases in time-versus-distance graphs, models K2 (Fig. 4), K2_SH20_I4 (Fig. 7b), K2_B6 (Fig. 9) and K2_SH20_B1 (Fig. 10b). The injection rate is shown by grey lines. The dots (individual earthquakes) are colour coded for magnitude.

linear trend of seismicity migration that may be related to the fracture opening and reopening. Conceptually, our single-fault core model corresponds to the latter situation.

In our simulated system, we find that the evolution of fault permeability is essential. We have considered the hypothesis in which the permeability immediately increases after fracturing and gradually decreases with time, given by the simple constitutive relations in eqs (19) and (23). The form of these equations is still to be explored, as many researchers propose different evolution laws and extreme values are possible (e.g. Miller & Nur 2000); this said, our idea is qualitatively consistent with earlier conceptions (e.g. Miller & Nur 2000). But permeability may increase even before or during rupture, and aseismic slip is possible (Calò *et al*. 2011). We have simplified our 3-D system to a projected 2-D fault model using the hypothesis that fluid migration and fault movement occur dominantly within a fault core. All of the injected fluid mass must circulate within the fault core along the fault plane and no loss is allowed off plane. No extraction from other wells is considered but further studies would be called for. In the field, the seismicity may not always be aligned on a single plane but it may be clustered in a 3-D volume. We also find that the pore pressure sometimes becomes extremely high when the given injection rate, permeability, porosity and fault width are not suitable. However, in a real system there should be some mechanical feedbacks between these parameters as well as an off-plane loss mechanism to keep pore pressure reasonable at any given time.

6 CONCLUSION

We developed a system of equations describing fluid migration, fault rheology and shear rupture. Assuming that the phenomena predominantly take place on a single fault with a finite permeable zone of variable width, we are able to project the volumetric fault core equations onto the 2-D fault plane by introducing a redefined boundary condition of eq. (10). Then we propose a toggle-switch type evolution of fault core permeability, eq. (19), and a healing process, eq. (23). Several parametric studies are performed to understand the basic behaviour of the system established by injecting the fluid at a single point. Fault rheology is a key element. In the absence of fault healing (no decrease in permeability) after rupture, seismicity is generally self-induced, for example, tends to evolve spontaneously once it is triggered, independently of the injection, and the fluid is completely drained. However, when a sufficiently rapid healing process takes place, the fluid mass is locally trapped along the fault and rupture migration can occur repeatedly. The pore pressure remains high after the end of the injection. The effect of segmentation of stress redistribution in the simulation has been studied and, in such cases, the system is sensitive to the injection protocol.

In this study, we have not precisely calibrated each parameter for specific examples of induced seismicity. The model developed in this study is general for different aspects of seismicity, such as plate boundaries, which may involve large amounts of fluid, as well as for earthquakes induced following injection or extraction of fluid or gas into or out of reservoirs.

ACKNOWLEDGEMENTS

We deeply regret that Dr Blanche Poisson passed away at the age of only 36 years on 2011 December 8. We would like to acknowledge her important contribution to the early stages of this study. The final version of the article was revised by the other four authors. We thank two anonymous reviewers for their comments, which have significantly improved the manuscript. This work was undertaken in the framework of the French national project ANR SUPNAF (2009–2011) and subsequently has been conducted under the European project FP7 GEISER (2010–2013) and Labex G-EAU-THERMIE PROFONDE. We also acknowledge the support of the INSU programs DyETI, CESSUR and NEEDS MIPOR, the ANR LANDQUAKE, the ITN FLOWTRANS and REALISE, a regional Alsatian program. We have also benefited from the support of BRGM funding. Finally, we thank John Douglas for proof reading.

REFERENCES

Aki, K., 1979. Characterization of barriers of an earthquake fault, *J. geophys. Res.,* **84,** 6140–6148.

Andrews, D.J., 2002. A fault constitutive relation accounting for thermal pressurization of pore fluid, *J. geophys. Res.,* **107,** 2363, doi:10.1029/2002JB001942.

Aochi, H. & Ide, S., 2009. Complexity in earthquake sequences controlled by multiscale heterogeneity in fault fracture energy, *J. geophys. Res.,* **114,** B03305, doi:10.1029/2008JB006034.

Aochi, H. & Matsu'ura, M., 2002. Slip- and time-dependent fault constitutive law and its significance in earthquake generation cycles, *Pageoph,* **159,** 2029–2044.

Audin, L., Avouac, J.-P., Flouzat, M. & Plantet, J.-L., 2002. Fluid-driven seismicity in a stable tectonic context: the Remiremont fault zone, Vosges, France, *Geophys. Res. Lett.,* **29**(6), 1091, doi:10.1029/2001GL012988.

Baisch, S. *et al.*, 2009. Deep heat mining basel—seismic risk analysis. Report of SERIANEX project. Available at: http://www.wsu.bs.ch/serianex_teil_1_english.pdf.

Baisch, S., Vörös, R., Rothert, E., Stang, H., Jung, R. & Schellschmidt, R., 2010. A numerical model for fluid injection induced seismicity at Soultz-sous-Forêts, *Int. J. Rock Mech. Min. Sci.,* **47,** 405–413.

Bak, P. & Tang, C., 1989. Earthquakes as self-organized critical phenomena, *J. geophys. Res.,* **94,** 15 635–15 637.

Beauce, A., Fabriol, F., LeMasne, D., Cavoit, C., Mechier, P. & Chen, X.K., 1991. Seismic studies on the HDR site of Soultz-Forêts (Alsace, France), *Geotherm. Sci. Tech.,* **3,** 239–266.

Bernabé, Y., Mok, U. & Evans, B., 2003. Permeability-porosity relationships in rocks subjected to various evolution processes, *Pure appl. Geophys.,* **160,** 937–960.

Blanpied, M.L., Lockner, D.A. & Byerlee, J.D., 1992. An earthquake mechanism based on rapid sealing of faults, *Nature,* **358,** 574–576.

Brace, W.F., 1977. Permeability from resistivity and pore shape, *J. geophys. Res.,* **82,** 3343–3349.

Brantut, N., Sulem, J. & Schubnel, A., 2011. Effect of dehydration reactions on earthquake nucleation: stable sliding, slow transients, and unstable slip, *J. geophys. Res.,* **116,** B05304, doi:10.1029/2010JB007876.

Bruel, D., 2002. Impact of induced thermal stresses during circulation tests in an engineered fracture geothermal reservoir, *Oil Gas Sci. Tech. Rev. IFP,* **57,** 459–470.

Bruel, D., 2007. Using the migration of the induced seismicity as a constraint for fracture Hot Dry Rock reservoir modelling, *Int. J. Rock Mech. Min. Sci.,* **44,** 1106–1117.

Caine, J.S., Evans, J.P. & Foster, C.G., 1996. Fault zone architecture and permeability structures, *Geology,* **24**(11), 1025–1028.

Calò, M., Dorbath, C., Cornet, F.H. & Cuenot, N., 2011. Large-scale aseismic motion identified through 4-D P-wave tomography, *Geophys. J. Int.,* **186,** 1295–1314.

Cappa, F. & Rutqvist, J., 2011a. Modeling of coupled deformation and permeability evolution during fault reactivation induced by deep underground injection of CO_2, *Int. J. Greenhouse Gas Control,* **5,** 336–346.

Cappa, F. & Rutqvist, J., 2011b. Impact of CO_2 geological sequestration on the nucleation of earthquakes, *Geophys. Res. Lett.,* **38,** L17313, doi:10.1029/2011GL048487.

Cappa, F. & Rutqvist, J., 2012. Seismic rupture and ground accelerations induced by CO_2 injection in the shallow crust, *Geophys. J. Int.,* **190,** 1784–1789.

Cappa, F., Rutqvist, J. & Yamamoto, K., 2009. Modeling crustal deformation and rupture processes related to upwelling of deep CO_2 rich fluids during the 1965–1967 Matsushiro Earthquake Swarm in Japan, *J. geophys. Res.,* **114,** B10304, doi:10.1029/2009JB006398.

Carman, P.C., 1937. Fluid flow through granular beds, *Trans. Inst. Chem. Eng., Lond.,* **15,** 150–166.

Chapman, R.E., 1981. *Geology and Water,* Kluwer.

Cheng, X., Xu, L., Patterson, A., Jaeger, H.M. & Nagel, S.R., 2008. Towards the zero-surface-tension limit in granular fingering instability, *Nat. Phys.,* **4,** 234–237.

Chester, F.M., Evans, J.P. & Biegel, R.L., 1993. Internal structure and weakening mechanisms of the San-Andreas fault, *J. geophys. Res.,* **98,** 771–786.

Cornet, F.H. & Jianmin, Y., 1995. Analysis of induced seismicity for stress field determination and pore pressure mapping, *Pageoph,* **145,** 677–700.

Dieterich, J., 1972. Time-dependent friction in rocks, *J. geophys. Res.,* **77,** 3690–3697.

Dorbath, L., Cuenot, N., Genter, A. & Frogneux, M., 2009. Seismic response of the fractured and faulted granite of Soultz-sous-Forêts (France) to 5 km deep massive water injections, *Geophys. J. Int.,* **177,** 653–675.

Evans, K.F. *et al.*, 2005. Microseismicity and permeability enhancement of hydrogeologic structures during massive fluid injection into granite at 3 km depth at the Soultz HDR site, *Geophys. J. Int.,* **160,** 388–412.

Evans, K.F., Zappone, A., Kraft, T., Deichmann, N. & Moia, F., 2012. A survey of the induced seismic responses to fluid injection in geothermal and CO_2 reservoirs in Europe, *Geothermics,* **41,** 30–54.

Fabriol, H., Beauce, A., Genter, A. & Jones, R., 1994. Induced microseismicity and its relation with naural fractures: the HDR example of Soultz (France), *Geotherm. Res. Counc. Trans.,* **18,** 423–430.

Flekkøy, E.G., Malthe-Sørenssen, A. & Jamtveit, B., 2002. Modeling hydrofracture, *J. geophys. Res.,* **107,** B2151, doi:10.1029/2000JB000132.

Garcia, R., Natale, G., Monnin, M. & Seidel, J.L., 2000. Shock wave radon surface signals associated with the upsurge of T-P solitons in volcanic systems, *J. Vol. Geotherm. Res.,* **96**(1–2), 15–24.

Gentier, S., Rachez, X., Peter-Borie, M. & Blaisonneau, A., 2011a. Hydraulic stimulation of geothermal wells: modeling of the hydro-mechanical behavior of a stimulated fractured rock mass, in *tProceedings of the XII International Congress of Rock Mechanics,* Beijing, China.

Gentier, S., Rachez, X., Peter-Borie, M., Blaisonneau, A. & Sanjuan, B., 2011b. Transport and flow modelling of the deep geothermal exchanger between wells and Soultz-sous-Forêts (France), *in Proceeding of the Geothermal Resources Council (GRC) Annual Meeting,* San Diego, California.

Ghani, I., Koehn, D., Toussaint, R. & Passchier, C.W., 2013. Dynamic development of hydrofracture, *Pure appl. Geophys.,* in press, doi:10.1007/s00024-012-0637-7.

Goren, L., Aharonov, E., Sparks, D. & Toussaint, R., 2010. The mechanics of pore fluid pressurization in deforming fluid-filled granular material, *J. geophys. Res.,* **115,** B09216, doi:10.1029/2009JB007191.

Goren, L., Aharonov, E., Sparks, D. & Toussaint, R., 2011. The mechanical coupling of fluid-filled granular material under shear, *P. A. Geophys.,* **168**(12), 2289–2323.

Gratier, J.-P., 2011. Fault permeability and strength evolution related to fracturing and healing episodic processes (years to millennia): the role of pressure solution, *Oil Gas Sci. Technol. Revue d'IFP Energies Nouvelles,* **66**(3), 491–506.

Gratier, J.-P., Richard, J., Renard, F., Mittempergher, S., Doan, M.L., Di Toro, G., Hadizadeh, J. & Boullier, A.M., 2011. Aseismic sliding of active faults by pressure solution creep: evidence from the San Andreas Fault Observatory at Depth, *Geology,* **39**(12), 1131–1134.

Gutenberg, B. & Richter, C.F., 1954. *Seismicity of the Earth and Associated Phenomena,* 2nd edn, Princeton University Press.

Hill, D.P. *et al.*, 1993. Seismicity remotely trigerred by the magnitude 7.3 Landers, California, earthquake, *Science,* **260,** 1617–1623.

Huang, H., Zhang, F., Callahan, P. & Ayoub, J., 2012a. Fluid injection experiments in 2D porous media, *SPE J.,* **17**(3), 903–911.

Huang, H., Zhang, F., Callahan, P. & Ayoub, J., 2012b. Granular fingering in fluid injection into Dense Granular media in a Hele-Shaw cell, *Phys. Rev. Lett.,* **108,** 258001, doi:10.1103/PhysRevLett.108.258001.

Ida, Y., 1972. Cohesive force across the tip of a longitudinal-shear crack and Griffith's specific surface energy, *J. geophys. Res.,* **77,** 3796–3805.

Ide, S. & Aochi, H., 2005. Earthquake as multiscal dynamic ruptures with heterogeneous fracture surface energy, *J. geophys. Res.,* **110,** B11303, doi:10.1029/2004JB003591.

Ide, S. & Takeo, M., 1997. Determination of constitutive relations of fault slip based on seismic wave analysis, *J. geophys. Res.,* **102**(B12), 27 379–27 391.

Iverson, R.M., 1997. The physics of debris flows, *Rev. Geophys.,* **35,** 245–296.

Johnsen, Ø., Toussaint, R., Måløy, K.J. & Flekkøy, E.G., 2006. Pattern formation during central air injection into granular materials confined in a circular Hele-Shaw cell, *Phys. Rev. E,* **74,** 011301, doi:10.1103/PhysRevE.74.011301.

Johnsen, Ø., Toussaint, R., Måløy, K.J., Flekkøy, E.G. & Schmittbuhl, J., 2008a. Coupled air/granular flow in a linear Hele-Shaw cell, *Phys Rev E,* **77,** 011301, doi:10.1103/PhysRevE.77.011301.

Johnsen, Ø., Chevalier, C., Lindner, A., Toussaint, R., Clément, E., Måløy, K.J., Flekkøy, E.G. & Schmittbuhl, J., 2008b. Decompaction and fluidization of a saturated and confined granular medium by injection of a viscous liquid or a gas, *Phys. Rev. E,* **78,** 051302, doi:10.1103/PhysRevE.78.051302.

Kaiser, J., 1950. Untersurchungenüber das Auftreten von GeräuschenbeimZugversuch, *PhD thesis,* Fak. F. Maschinenwesen, TH München, Germany.

Kanamori, H. & Anderson, D., 1975. Theoretical basis of some empirical relations in seismology, *Bull. seism. Soc. Am.,* **65,** 1073–1095.

Kanamori, H. & Stewart, G.S., 1978. Seismological aspects of the Guatemala earthquake of February 4, 1976, *J. geophys. Res.,* **83,** 3427–3434.

Kappeimeyer, O., Gérard, A., Schloemer, W., Ferrandes, R., Rummel, F. & Benderitter, Y., 1991. European HDR project at Soultz-sous-Forêts general presentation, *Geotherm. Sci. Tech.,* **2,** 263–289.

Karabulut, H. *et al.*, 2011. Evolution of the seismicity in the eastern Marmara Sea a decade before and after the 17 August 1999 Izmit earthquake, *Tectonophysics*, **510,** 17–27.

Kozeny, J., 1927. Ueber kapillare Leifung des Wassers im Boden, Sitzungsber Akad. Wiss., Wien, **136**(2a), 271–306.

Lockner, D.A., Tanaka, H., Ito, H., Ikeda, R., Omura, K. & Naka, H., 2009. Geometry of the Nojima fault at Nojima-Hirabayashi, Japan—I. A simple damage structure inferred from borehole core permeability, *Pure appl. Geophys.,* **166,** 1649–1667.

Lombardi, A.M., Cocco, M. & Marzocchi, W., 2010. On the increase of background seismicity rate during the 1997–1998 Umbria-Marche, Central Italy, sequence: apparent variation or fluid-driven triggering? *Bull. seism. Soc. Am.,* **100,** 1138–1152.

Løvoll, G., Méheust, Y., Toussaint, R., Schmittbuhl, J. & Måløy, K.J., 2004. Growth activity during fingering in a porous Hele Shaw cell, *Phys. Rev. E.,* **70,** 026301, doi:10.1103/PhysRevE.70.026301.

Mai, P.M. & Beroza, G.C., 2002. A spatial random field model to characterize complexity in earthquake slip, *J. geophys. Res.,* **107,** 2308, doi:10.1029/2001JB000588.

Majer, E.L., Baria, R., Stark, M., Oates, S., Bommer, J., Smith, B. & Asanuma, H., 2007. Induced seismicity associated with enhanced geothermal systems, *Geothermics,* **36,** 185–222.

Majer, E., Nelson, J., Robertson-Tait, A., Savy, J. & Wong, I., 2012. Protocol for addressing induced seismicity associated with enhanced geothermal systems, U.S. Department of Energy, DOE/EE-0662.

Matsu'ura, R.S. & Karakama, I., 2005. A point-process analysis of the Matsushiro earthquake swarm sequence: the effect of water on earthquake occurrence, *Pure appl. Geophys.,* **162,** 1319–1345.

Mavko, G., Mukerli, T. & Dvorkin, J., 2009. *The Rock Physics Handbook, Tools for Seismic Analysis of Porous Media,* 2nd edn, Cambridge University Press.

Mazzoldi,, A., Rinaldi, A.P., Borgia, A. & Rutqvist, J., 2012. Induced seismicity within geologic carbon sequestration projects: maximum earthquake magnitude and leakage potential, *Int. J. Greenhouse Gas Control,* **10,** 434–442.

Miller, S.A. & Nur, A., 2000. Permeability as a toggle swith in fluid-controlled crustal processes, *Earth planet. Sci. Lett.,* **183,** 133–146.

Miller, S., Nur, A. & Olgaard, D., 1996. Earthquakes as a coupled shear stress-high pore pressure dynamical system, *Geophys. Res. Lett.,* **23,** 197–200.

Miller, S.A., Collettini, C., Chiaraluce, L., Cocco, M., Barchi, M. & Kaus, B.J.P., 2004. Aftershocks driven by a high-pressure CO_2 source at depth, *Nature,* **427,** 724–727.

Nakatani, M., 1997. Experimental study of time-dependent phenomena in frictional faults as a manifestation of stress-dependent thermally activated process, *PhD thesis*, The University of Tokyo.

Neuville, A., Toussaint, R. & Schmittbuhl, J., 2009. Fracture roughness and thermal exchange: a case study at Soultz-sous-Forets, C.R.A.S., *Geoscience,* **342,** 616, doi:10.1016/j.crte.2009.03.006.

Niebling, M.J., Flekkøy, E.G., Måløy, K.J. & Toussaint, R., 2010a. Sedimentation instabilities: impact of the fluid compressibility and viscosity, *Phys. Rev. E,* **82,** 051302, doi:10.1103/PhysRevE.82.051302.

Niebling, M.J., Flekkøy, E.G., Måløy, K.J. & Toussaint, R., 2010b. Mixing of a granular layer falling through a fluid, *Phys. Rev. E,* **82,** 011301, doi:10.1103/PhysRevE.82.011301.

Niebling, M., Toussaint, R., Flekkøy, E.G. & Måløy, K.J., 2012a. Estudios numéricos de Aerofractures en medios poros / Numerical studies of aerofractures in porous media, *Revista Cubana de Fisica,* **29,** 1E, 1E66.

Niebling, M.J., Toussaint, R., Flekkøy, E.G. & Måløy, K.J., 2012b. Dynamic aerofracture of dense granular packings, *Phys. Rev. E,* **86,** 061315, doi:10.1103/PhysRevE.86.061315.

Nur, A. & Byerlee, J.D., 1971. An exact effective stress law for elastic deformation of rock with fluids, *J. geophys. Res.,* **76**(26), 6414–6419.

Obara, K., 2002. Nonvolcanic deep tremor associated with subduction in southwest Japan, *Science,* **296,** 1679–1681.

O'Connell, R.J. & Budiansky, B., 1974. Seismic velocities in dry and saturated cracked solids, *J. geophys. Res.,* **79,** 5412–5426.

Ohnaka, M., 2003. A constitutive scaling law and a unified comprehension for frictional slip failure, shear fracture of intact rock, and earthquake rupture, *J. geophys. Res.,* **108**(B2), 2080, doi:10.1029/2000JB000123.

Ohtake, M., 1976. A review of the Matsushiro earthquake swarm, *Kagaku,* **46,** 306–313 (in Japanese).

Palmer, A.C. & Rice, J.R., 1973. The growth of slip surfaces in the progressive failure of over-consolidated clay, *Proc. R. Soc. Lond. A,* **332,** 527–548.

Perfettini, H., Schmittbuhl, J. & Vilotte, J.P., 2001. Slip correlations on a creeping fault, *Geophys. Res. Lett.,* **28**(10), 2137–2140.

Person, C., 1981. The relationship between microseismicity and high pore pressure during hydraulic stimulation experiments in low permeability granite rocks, *J. geophys. Res.,* **86,** 7855–7864.

Revil, A., 2002. Genesis of mud volcanoes in sedimentary basins: a solitary wave-based mechanism, *Geophys. Res. Lett.,* **29,** 12, doi:10.1029/2001GL014465.

Rice, J.R., 1993. Spatio-temporal complexity of slip on a fault, *J. geophys. Res.,* **98,** 9885–9907.

Rice, J.R., 2006. Heating and weakening of faults during earthquake slip, *J. geophys. Res.,* **111,** B05311, doi:10.1029/2005JB004006.

Rozhko, A.Y., 2010. Role of seepage forces on seismicity triggering, *J. geophys. Res.,* **115,** B11314, doi:10.1029/2009JB007182.

Schelstraete, M., 2009. Suivi de la décompaction et aérofracturation de matériaux faiblement consolidés, *Masters thesis*, University of Strasbourg, France.

Schmittbuhl, J., Vilotte, J.P. & Roux, S., 1993. Propagative macrodislocation modes in an earthquake fault model, *Europhys. Lett.,* **21,** 375–380.

Schmittbuhl, J., Chambon, G., Hansen, A. & Bouchon, M., 2006. Are stress distributions along faults the signature of asperity squeeze? *Geophys. Res. Lett.*, **33,** L3307, doi:10.1029/2006GL025952.

Segall, P. & Rice, J.R., 1995. Dilatancy, compaction and slip instability of a fluid-infiltrated fault, *J. geophys. Res.,* **100,** 22 155–22 171.

Segall, P. & Rice, J.R., 2006. Does shear heating of pore fluid contribute to earthquake nucleation? *J. geophys. Res.,* **111,** B09316, doi:10.1029/2005JB004129.

Shapiro, S.A. & Dinske, C., 2009. Fluid-induced seismicity: pressure diffusion and hydraulic fracturing, *Geophys. Prospect.,* **57,** 301–310.

Shapiro, S.A., Audigane, P. & Royer, J.-J., 1999. Large-scale in situ permeability tensor of rocks from induced microseismicity, *Geophys. J. Int.,* **137,** 207–213.

Tada, T., Fukuyama, E. & Madariaga, R., 2000. Non-hypersingular boundary integral equations for 3-D non-planar crack dynamics, *Comput. Mech.,* **25,** 613–626.

Terakawa, T., Zoporowski, A., Galvan, B. & Miller, S.A., 2010. High-pressure fluid at hypocentral depths in the L'Aquila region inferred from earthquake focal mechanisms, *Geology,* **38,** 995–998.

Terzaghi, K., 1943. *Theoretical Soil Mechanics,* John Wiley and Sons.

Thurber, C., Roecker, S., Ellsworth, W., Chen, Y., Lutter, W. & Sessions, R., 1997. Two-dimensional seismic image of the San Andreas fault in the northern Gabilan range, central California: evidence for fluids in the fault zone, *Geophys. Res. Lett.,* **24,** 1591–1594.

Vinningland, J.L., Johnsen, Ø., Flekkøy, E.G., Toussaint, R. & Måløy, K.J., 2007a. A granular Rayleigh-Taylor instability: experiments and simulations, *Phys. Rev. Lett.,* **99,** 048001, doi:10.1103/PhysRevLett.99.048001.

Vinningland, J.L., Johnsen, Ø., Flekkøy, E.G., Toussaint, R. & Måløy, K.J., 2007b. Experiments and simulations of a gravitational granular flow instability, *Phys. Rev. E,* **76,** 051306, doi:10.1103/PhysRevE.76.051306.

Vinningland, J.L., Johnsen, Ø., Flekkøy, E.G., Toussaint, R. & Måløy, K.J., 2010. Size invariance of the granular Rayleigh-Taylor instability, *Phys. Rev. E,* **81,** 041308, doi:10.1103/PhysRevE.81.041308.

Vinningland, J.L., Toussaint, R., Niebling, M., Flekkøy, E.G. & Måløy, K.J., 2012. Family-Vicsek scaling of detachment fronts in Granular Rayleigh

Taylor instabilities during sedimenting granular/fluid flows, *Eur. Phys. J.-Spec. Top.,* **204**(1), 27–40.
Walder, J. & Nur, A., 1984. Porosity reduction and crustal pore pressure development, *J. geophys. Res.,* **89,** 11 539–11 548.
Wong, T.-F., Ko, S.-C. & Olgaard, D.L., 1997. Generation and maintenance of pore pressure excess in a dehydrating system, 2. Theoretical analysis, *J. geophys. Res.,* **102,** 841–852.
Yamashita, T., 1999. Pore creation due to fault slip in a fluid-permeated fault zone and its effect on seismicity, *Pure appl. Geophys.,* **155,** 625–647.
Zimmerman, R.W. & Bodvarsson, G.S., 1996. Effective transmissivity of a two-dimensional fracture network, *Int. J. Rock Mech.,* **33,** 433–438.
Zimmerman, R.W. & Main, I.G., 2004. Hydromechanical behaviour of fractured rocks, in *Mechanics of Fluid-Saturated Rocks,* pp. 363–421, eds. Gueguen, Y. & Bouteca, M., Academic Press.
Zoback, M.D. & Gorelick, S.M., 2012. Earthquake triggering and large scale geologic storage of carbon dioxide, *Proc. Natl. Acad. Sci. U.S.A.,* **109**(26), 10164–10168.

APPENDIX A: ELASTIC EQUATION FOR STRESS REDISTRIBUTION

The theory of the linear static elasticity gives us a unique solution based on the equilibrium theory. The stress change at any place in the medium is written as a convolution of the causal fault slip over and the response function (Green's function), G, 'on' the whole area of the fault (Σ):

$$\Delta\tau(\vec{x}) = \int_{\Sigma} G(\vec{x}-\vec{\xi})\Delta u(\vec{\xi})\,\mathrm{d}\Sigma. \tag{A1}$$

The response function G has symmetry with respect to the relative location $(\vec{x}-\vec{\xi})$. Let us discuss only on a fault plane ($z=0$) and discretize (x, y)-fault plane in squares of the equal size: $\vec{x} = (i\Delta s,\ j\Delta s, 0)$ and $\vec{\xi} = (l\Delta s,\ m\Delta s, 0)$. Then we can write (A1) as

$$\Delta\tau_{ij} = \sum_{l,m} G_{(i-l)(j-m)}\Delta u_{lm}. \tag{A2}$$

Tada *et al.* (2000) provide the analytical solution for the 3-D homogeneous, elastic, isotropic medium. For a dislocation in the x-direction, shear stress in xz-component is written as:

$$\Delta\tau(\vec{x}) = -\frac{\mu}{4\pi}\int_{\Sigma}\mathrm{d}\Sigma\left[2(1-p^2)\frac{\gamma_1}{r^2}\frac{\partial\Delta u}{\partial x} + \frac{\gamma_2}{r^2}\frac{\partial\Delta u}{\partial y}\right], \tag{A3}$$

where $p^2 = \beta^2/\alpha^2$ (α, P-wave velocity; β, S-wave velocity), $r^2 = |\vec{x}-\vec{\xi}|^2$ and $\gamma_i = (x_i-\xi_i)/r$. In such boundary integral equation formulations, slip on an element is usually assumed uniform:

$$\begin{aligned}\Delta u(\vec{\xi}) = \Delta u_{lm}\,[&H(\xi_1-(l-1/2)\Delta s)H(\xi_2-(m-1/2)\Delta s)\\ &- H(\xi_1-(l-1/2)\Delta s)H(\xi_2-(m+1/2)\Delta s)\\ &- H(\xi_1-(l+1/2)\Delta s)H(\xi_2-(m-1/2)\Delta s)\\ &+ H(\xi_1-(l+1/2)\Delta s)H(\xi_2-(m+1/2)\Delta s)],\end{aligned} \tag{A4}$$

and we estimate the stress at the centre of each element $(i\Delta s,\ j\Delta s)$. We can obtain the analytical solution from (A3) for a unit slip $\Delta u = \Delta u\cdot H(x_1)H(x_2)$:

$$\Delta\tau(\vec{x}) = -\frac{\mu\Delta u}{4\pi}\left[\frac{1}{\sqrt{x_1^2+x_2^2}}\left\{2(1-p^2)\frac{x_2}{x_1}+\frac{x_1}{x_2}\right\} - \left\{2(1-p^2)\frac{1}{x_1}+\frac{1}{x_2}\right\}\right]. \tag{A5}$$

Consequently, we can obtain the response function for eq. (A4) by combining the solution (A5), as illustrated in Fig. A1. Note that, the stress remains finite at any collocation points, including on the causal source element (0, 0) and the neighbouring elements (±1, ±1). The detailed derivation of the equations is given in Tada *et al.* (2000).

APPENDIX B: RESOLUTION IN NUMERICAL SIMULATIONS

In the overall study, we suppose an element size of 30 m, which allows a minimum earthquake of about M 1.3 under the given friction law, namely eq. (16). As the system of the equations is a highly non-linear self-organizing system, we are concerned about the resolution of the numerical simulations seen at different scales. Fig. A2 represents a simulation with a grid size of 50 m (time step of 2 s) for the same physical parameters used in Fig. 4. As expected, the minimum magnitude appearing during the simulation increases to about 1.8, namely smaller earthquakes than this are not modelled. Consequently, the number of earthquakes decreases. Due to the non-linearlity and different discretization, we may not find

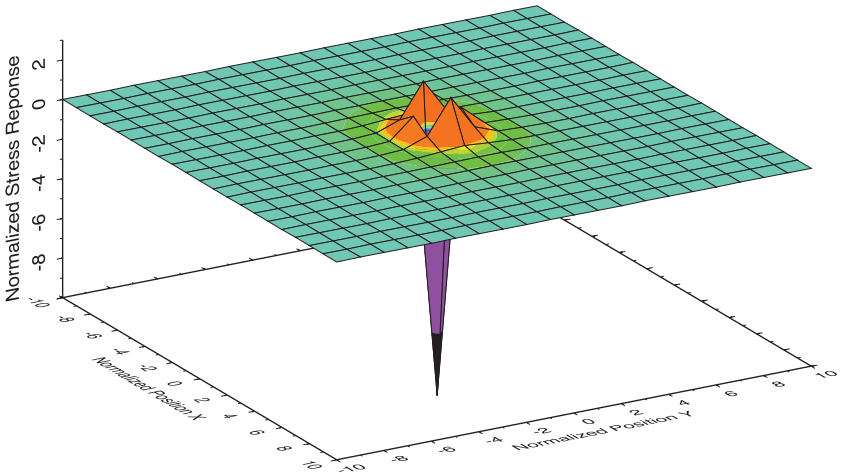

Figure A1. Shear stress redistribution in the 3-D homogeneous elastic medium due to a dislocation (slip direction is parallel to the x-axis) located at the centre of the fault plane. All the axes are normalized.

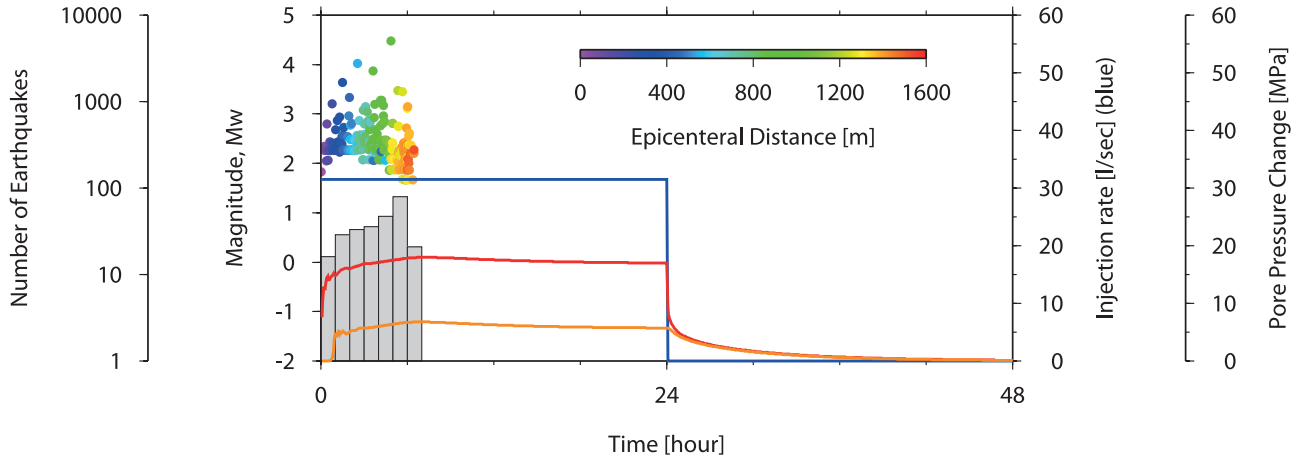

Figure A2. The same situation as model K2 in Fig. 4 but with an element size of 50 m for checking the numerical resolution. The statistical feature of the appearing seismicity and the fluid circulation are consistent in the both simulations. For notations, see also the caption for Fig. 3.

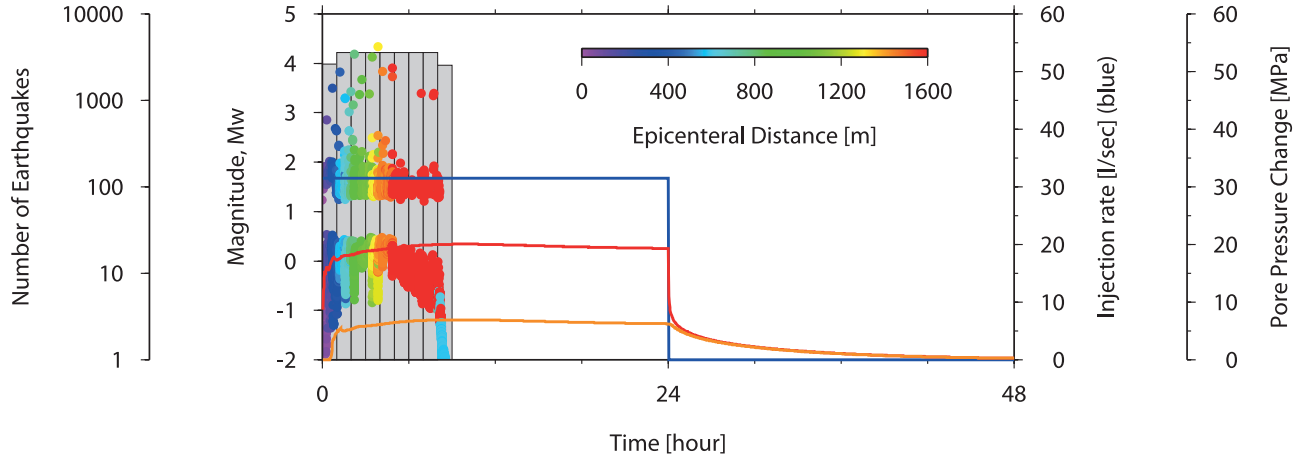

Figure A3. The same situation as model K2 in Fig. 4 but with a critical slip displacement D_c of 0.01 m.

the same earthquake (epicentre location, magnitude, time, etc.) in a deterministic manner, strictly speaking. However, the statistical features of the seismicity are the same. The seismicity propagates outwards and then we find a maximum event of M_w 4.47 at 4.9 hr after the injection start (previously M_w 4.52 at 4.1 hr in Fig. 4). Most of the seismicity is calmed after 6 hr. The pore pressures on the fault (lines in red and orange) show an identical behaviour at different points. These observations assure the coherence in our discussions on the statistical characters of the seismicity evolution and fluid circulation.

On the other hand, one may also pose a question about the slip-weakening distance (D_c) used in this study. We dare to take it very small, because we do not want to bring any complex discussion about its temporal evolution (e.g. Nakatani 1997; Aochi & Matsu'ura 2002) or its scaling problem (e.g. Ohnaka 2003; Aochi & Ide 2009). However, it is worth mentioning what may happen if we take a longer D_c. The fact of small D_c is that the rupture brings the totality of the stress drop described by eq. (15) regardless of the dimension of rupture (number of ruptured elements). This is why the smallest earthquakes are aligned around a magnitude 1.3. Later on, smaller earthquakes appear, because an increase in the pore pressure leads to a decrease in effective normal stress and consequently a smaller stress drop.

Fig. A3 represents a simulation assuming $D_c = 0.01$ [m] under the same configuration with Fig. 4. We note that $D_c = 0.01$ [m] is a reasonable value for an event of magnitude 4 (Ohnaka 2003; Ide & Aochi 2005). A long D_c allows a tiny displacement with a smaller stress drop (a very small magnitude event), and this generates only a slight stress concentration in the surrounding (schematic illustration in Fig. A4). In order to accumulate enough shear stress in the surrounding, many small earthquakes are required. On the other hand, as described in eq. (19), the permeability becomes immediately large once the concerned element is ruptured regardless of its slip amount. Thus, the fluid circulation may later on play a role in reducing the fault strength during the seismicity. As a result, the seismicity appearance becomes very complex, and their magnitude–frequency relation is not any more a continuous linear inverse relation. Taking into account a finite length of D_c is required particularly when considering a certain pre-fixed size of earthquake and its preparation process (e.g. towards a M 4 event in this case), however, this does not assure the self-organizing system of multiscale phenomena. For this purpose, one will have to carry out dynamic rupture simulations taking into account the inertia and

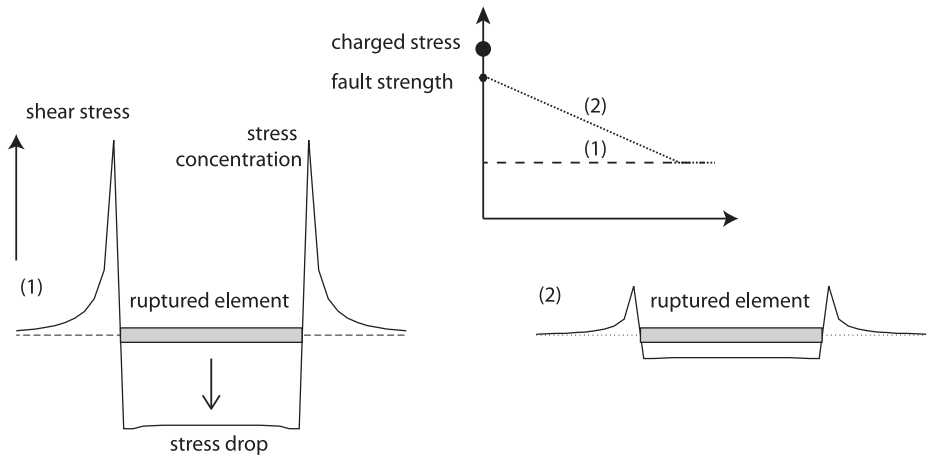

Figure A4. A schematic illustration of the stress release and redistribution in the cases of (1) immediate stress drop (D_c small enough) and (2) a longer D_c. As illustrated at the top corner, the slope (grey line) of the relaxation is determined by the system of the elastic equations. The discrepancy between the charged shear stress and the fault strength is equilibrated by an increment slip. Namely the equilibrium state is the cross between the relaxation line (solid grey) and the friction lines (dotted or broken lines). If D_c is small enough, frictional slope is steeper than the grey line, so that the system always finds the equilibrium state at the residual level of friction, as line (1). Besides, when D_c is large enough, such as case (2), the equilibrium state is found with a small amount of stress drop and fault slip. As a result, stress concentration in the surrounding is large in case (1) comparing to case (2).

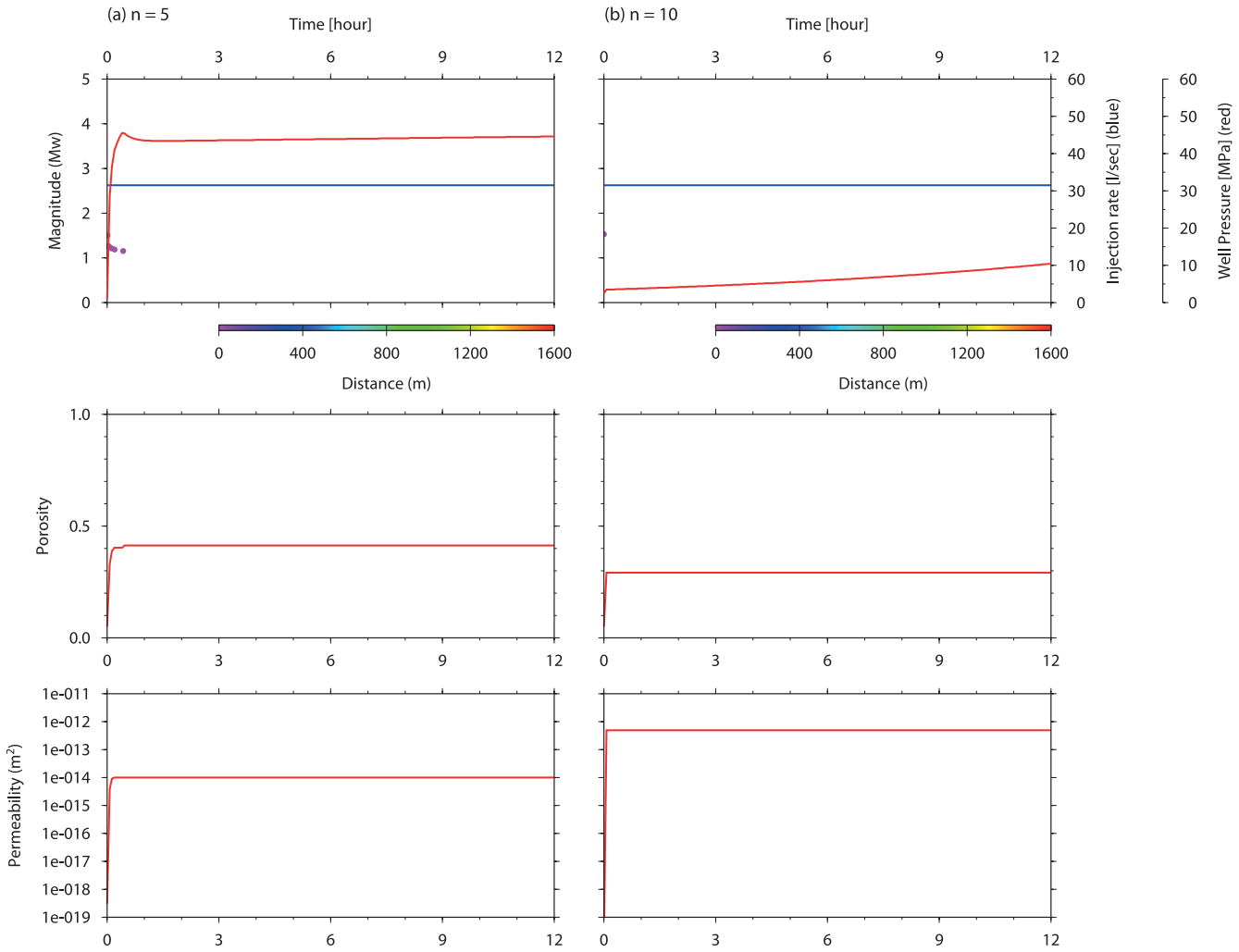

Figure A5. Simulation results for (a) $n = 5$ and (b) $n = 10$, respectively. On the top, injection rate (blue lines), the resultant seismicity (colour circles) and the pore pressure change (red lines) at the injection point are shown in function of time. In the middle and bottom panels, porosity and permeability at the injection point are shown. The porosity change is saturated to the given upper limit.

scaling problem (e.g. Aochi & Ide 2009). However, for the purpose of this study and for the simplicity of the later discussion, we adopt the assumption that D_c is small enough to let the complete stress drop every time.

APPENDIX C: PRELIMINARY ATTEMPT ON FAULT EVOLUTION

As our preliminary attempt, we have tested the continuous, relatively gentile, relations, eqs (17) and (18). In Fig. A5, we show two test cases in the first 12 hr during the continuous injection, supposing $u_c = 0.01$ m in eq. (17) and $n = 5$ or 10 in eq. (18). The porosity and the permeability are shown for the central element where the fluid is injected. In both cases, the system finds rapidly the equilibrium status (fluid circulates) after only a few events without any significant seismicity. As observed in the lower panels, the permeability and the porosity changes are so quick, and practically discontinuous, and are also saturated, as the porosity is forced to be limited to 0.45, although this sounds extremely large. As the rupture process is non-linear, the slip amount of successive events differ from each other are very difficult to control, while the relations such as eqs (17) and (18) are unique. These examples show the difficulty to control the fluid circulation in simple equations. Thus, we will adopt a discontinuous phase change in permeability change according to the rupturing.